GEOPHYSICS, VOL. 80, NO. 2 (MARCH-APRIL 2015); P. D111–D127, 19 FIGS., 1 TABLE.
10.1190/GEO2014-0335.1

Bulk modulus dispersion and attenuation in sandstones

L. Pimienta[1], J. Fortin[1], and Y. Guéguen[1]

ABSTRACT

We report experimental data on the frequency dependence of bulk elastic modulus in porous sandstones. A new methodology was developed to investigate the dispersion/attenuation phenomena on a rock's bulk modulus K for varying confining pressures in the range of 1–50 MPa and fluids of varying viscosities (i.e., air, glycerin, and water). This methodology combined (1) ultrasonic (i.e., $f \sim 0.5$ MHz) P- and S-wave velocity measurements, leading to the high-frequency (HF) K_{HF}, (2) stress-strain measurements from forced periodic oscillations of confining pressure at low-frequency (LF) ranges (i.e., $f \in [4\ 10^{-3}; 4\ 10^{-1}]$ Hz), leading to K_{LF} and Q_K^{-1}, and (3) pore-pressure measurement to document the induced fluid-flow in the LF range (i.e., $f \in [4\ 10^{-3}; 4\ 10^{-1}]$ Hz). The stress-strain method was first checked using three standard samples: glass, gypsum, and Plexiglas samples. Over the frequency and pressure range of the apparatus K_{LF} was stable and accurate and the lowest measurable LF attenuation was $Q_K^{-1} \sim 0.01$. The methodology was applied to investigate Fontainebleau sandstone samples of 7% and 9% porosity. The K_{LF} and Q_K^{-1} exhibited correlated variations, which also correlated with an experimental evidence of frequency-dependent fluid-flow out of the sample. Attenuation peaks as high as $Q_K^{-1} \sim 0.15$ and $Q_K^{-1} \sim 0.25$ are measured. The attenuation/dispersion measured under glycerin saturation was compared to Biot-Gassmann predictions. The overall behavior of one sample was consistent with a dispersion/attenuation characteristic of the drained/undrained transition. On the reverse, the other sample exhibited exotic behaviors as the measurements were underestimated by the drained/undrained transition and indicated a direct transition from drained to unrelaxed domain. These different behaviors were consistent with the values of the critical frequencies expected for the drained/undrained (i.e., f_1) and relaxed/unrelaxed (i.e., f_2) transitions.

INTRODUCTION

Comparing rocks' elastic properties inferred from either laboratory ultrasonic (i.e., $f \sim 1$ MHz) or field sonic (i.e., $f \in [1; 10^3]$ Hz) velocities is not straightforward because of the frequency range (i.e., up to five orders of magnitude). Frequency effects are expressed in terms of dispersion and attenuation of a wave traveling through a medium. Various theories were developed to understand and account for these effects in fluid-saturated porous rocks (e.g., O'Connell and Budiansky, 1974; Cleary, 1978; Winkler and Murphy III, 1995; Ravalec et al., 1996; Mavko et al., 2003; Müller et al., 2010; Adelinet et al., 2011). Overall, these theories aim at predicting the characteristic frequencies of the effect and the amplitude of attenuation and dispersion.

Even though frequency effects are shown to be important in partially saturated media (e.g., Tisato and Madonna, 2012; Madonna and Tisato, 2013), only fully saturated rocks are investigated here. In a fully saturated rock, three flow regimes are expected to take place in the frequency range of $f \in [10^{-2}; 10^6]$ Hz (e.g., Cleary, 1978; Sarout, 2012). The first regime is the drained one. It corresponds to a macroscopic fluid flow and is thus associated to very low frequency. The second regime is the undrained one. At a scale of a representative elementary volumes (REVs), there is an isobaric state but no macroscopic flow can occur. The drained and undrained regimes are well accounted for through quasistatic poroelasticity. By comparison with the first two regimes, both relaxed, the third regime is an unrelaxed one. It corresponds to a nonisobaric REV. It follows from the existence of these three regimes, of fluid flow that two transitions are expected: from drained to undrained regimes and from relaxed to unrelaxed regimes.

Several experiments aiming at measuring such effects in the laboratory have been performed in recent years (Subramaniyan et al.,

Manuscript received by the Editor 24 July 2014; revised manuscript received 10 November 2014; published online 2 February 2015.
[1]CNRS, PSL Research University, Laboratoire de Géologie de l'ENS, Paris, France. E-mail: pimienta@geologie.ens.fr; fortin@geologie.ens.fr; gueguen@geologie.ens.fr

2014). In particular, a "stress-strain" forced oscillation method has been introduced (e.g., Spencer, 1981). Axial forced oscillations have widely been used for measuring the Young modulus and attenuation for a frequency range of about $f \in [10^{-2}; 10^{3}]$ Hz (e.g., Adam et al., 2006; Batzle et al., 2006; Tisato and Madonna, 2012; Madonna and Tisato, 2013; Mikhaltsevitch et al., 2014). A similar method was used by Jackson and Paterson (1987) to determine shear dispersion and attenuation in the range of $f \in [0.01; 0.3]$ Hz with torsional forced oscillations. Measuring bulk modulus was made possible using confining pressure forced oscillations (Adelinet et al., 2010; David et al., 2013; Fortin et al., 2014). Adelinet et al. (2010) and David et al. (2013) compare the HF (i.e., $f \sim 1$ MHz) and LF (i.e., $f \sim 0.1$ Hz) bulk moduli of dry and fluid-saturated rocks. However, these authors do not investigate the variation in bulk modulus with frequency nor do they measure attenuation in this pressure oscillation mode.

The present contribution reports new results on frequency-dependent dispersion and attenuation on the bulk modulus. The experimental setup is first presented and calibrated using three standard samples. Then, results are reported for two Fontainebleau samples fully saturated with different fluids. The results are interpreted on the basis of the three fluid-flow regimes and their characteristic frequencies.

SAMPLES, EXPERIMENTAL APPARATUS, AND PROCEDURE

Samples studied

Calibration samples

Three standard samples were chosen to test the experimental setup and procedure: (1) a synthetic glass sample made of amorphous silica (Ougier-Simonin et al., 2011; Mallet et al., 2013), (2) a pure gypsum sample (Brantut et al., 2012), and (3) a Plexiglas (poly[methyl methacrylate] PMMA) sample (e.g., Batzle et al., 2006). These were chosen because (1) they are homogeneous and isotropic media at the sample scale; (2) their elastic properties are known, and they show a large range in compressibilities from $K = 4.5$ GPa for Plexiglas (e.g., Barrau and Laroze, 1988) to $K = 60$ GPa for glass (e.g., Ougier-Simonin et al., 2011); (3) these samples have a negligible porosity, and their elastic properties are not expected to change with confining pressure; and (4) even though glass and gypsum elastic properties are independent of frequency, Plexiglas is a viscoelastic material whose elastic properties are frequency dependent. Plexiglas is often used as a mean to test an attenuation apparatus (e.g., Batzle et al., 2006; Tisato and Madonna, 2012; Madonna and Tisato, 2013).

Fontainebleau samples

The Fontainebleau Sandstone is a well-known reference rock. The framework grains and cement are pure quartz, making up a clean sandstone of approximately 99.9% quartz (Bourbie and Zinszner, 1985; Gomez et al., 2010). Because the rock was formed from aeolian quartz grains deposited, the rock possesses a random grain orientation and is well sorted, with an average grain radius of approximately $r = 100$ μm. Figure 1 shows a Fontainebleau typical thin section. From Figure 1a, the rock can consistently be assumed to be homogeneous at the REV scale (i.e., volume ≫ grains' volume). Furthermore, by adding a polarizing prism (Figure 1b), it is shown that the different quartz grains have each a different orientation, making the isotropic assumption consistent for this rock.

Depending on the amount of quartz cement, Fontainebleau Sandstone porosity ranges from approximately $\phi \sim 2\%$ for highly cemented samples to approximately $\phi \sim 25\%$ for ill-cemented samples. The main differences between samples are the pores' entry diameters, leading to variations in permeability of approximately four to five orders of magnitude (Bourbie and Zinszner, 1985) between the extreme cases. The two samples chosen have porosities of approximately $\phi = 7.3\%$ (i.e., Fo7) and $\phi = 8.8\%$ (i.e., Fo9), respectively. Their total pore volume, measured from total fluid injection at lowest effective pressure, is of $V_{Fo7} \sim 7.2$ mL and $V_{Fo9} \sim 8.6$ mL, respectively. This is consistent with the samples' dimensions of 40-mm diameter and 80-mm length, i.e., rock volume of approximately ~100 mL. As documented by Bourbie

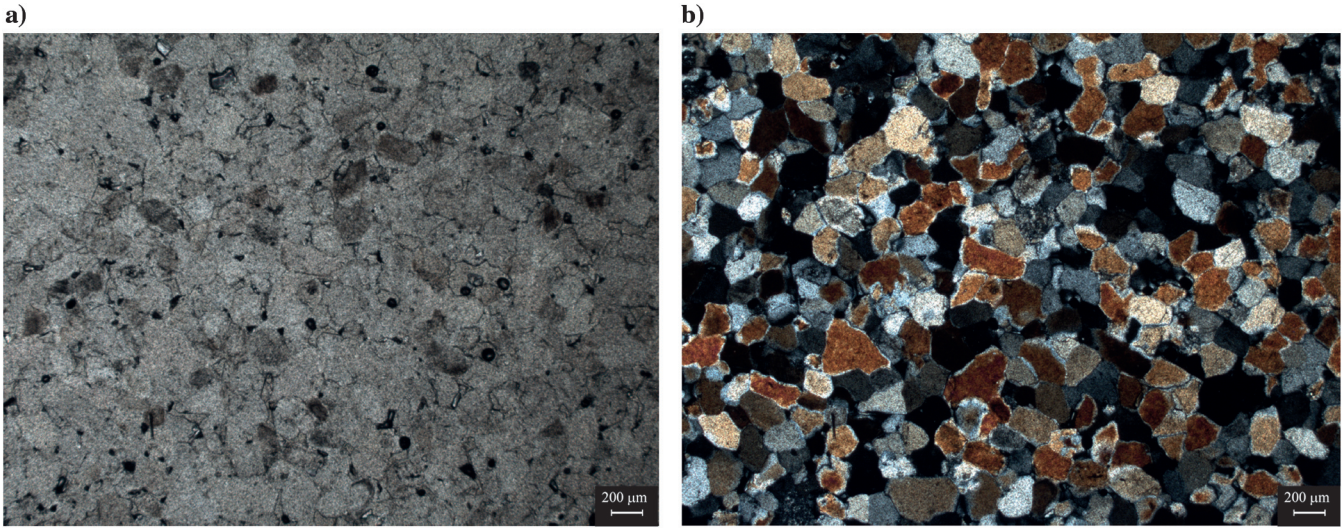

Figure 1. Microscopic image of a thin section of the approximately 7% Fontainebleau Sandstone (a) without and (b) with a polarizing prism. In panel (a), grains appear in gray and pores are in black. In panel (b), the colors come from the polarizing direction.

and Zinszner (1985), these samples of slightly different porosities are expected to fall in almost the same permeability range of approximately $\kappa \in [10^{-14}; 10^{-15}]$ m^2.

Experimental apparatus and procedure

Cell and confining setup

The apparatus aims at measuring simultaneously high-frequency (HF) and low-frequency (LF) elastic properties. To investigate these properties at different pressures, measurements are conducted in an oil-confining triaxial apparatus (Fortin et al., 2005) that can be used in two different setups thanks to an axial piston that can be shifted vertically. Only the first setup, in which the axial piston is not in contact with the end-platen (and thus the sample), is used here. It allows for studying the sample under pure isotropic conditions. For the sample to be isolated from the surrounding confining oil, it is jacketed radially and enclosed in two end-platens.

A servocontrolled confining pump is linked to the bottom of the cell chamber to deliver the confining pressure. The applied pressure is directly measured by a Keller pressure transducer with accuracy down to approximately $P_c \sim 0.01$ MPa. This pressure transducer is placed at the top of the chamber so that the pressure measurement is strictly equal to that applied to the sample.

Experimental procedure

A procedure (Figure 2) is devised to measure the rocks' bulk moduli using different fluids at different confining pressures. Starting from a pressure of approximately ~1 MPa, elastic moduli are measured at each loading step of confining pressure up to the maximum confining of ~50 MPa. For fluid saturation, the confining pressure is slowly decreased down to a pressure of approximately ~3 MPa. At this low pressure, a fluid (i.e., glycerin then water) is introduced in the sample. After pore pressure stabilization (i.e., $P_p \sim 2$ MPa), the properties are measured again. For the sandstone samples in fluid-saturated conditions, Terzaghi effective pressure $P_{\text{eff}} = P_c - P_p$ is used, which allows for comparison between dry and fluid-saturated conditions. This approximation of the effective pressure is chosen to report the data in a simple way.

The standard nonporous samples are measured in dry conditions only (i.e., step 1 in Figure 2). The Fontainebleau samples are measured under (1) dry, (2) glycerin full saturation, and (3) water full saturation conditions. Starting from the initial pressure of measurement, a controlled rate of approximately 0.01 MPa is used for loading and unloading as to allow for complete/instantaneous relaxation of the fluid-filled sample (Fortin et al., 2007; David et al., 2013).

At each confining pressure, LF and HF properties are obtained using two different methods (Figure 2). HF elastic properties (Figure 2b) are deduced from the measured ultrasonic wave velocities. LF properties (Figure 2a) are measured using confining pressure oscillations around a mean effective pressure value. The induced strain and pore pressure oscillations are recorded. The LF bulk modulus is deduced from the ratio of volumetric strain $\Delta\epsilon$ over confining ΔP_c oscillations. These oscillations are very small, i.e., $\Delta P_c \sim 0.2$ MPa.

The glycerin full saturation of the sample is ascertained by an injection procedure: (1) Vacuum is applied with a vacuum pump at the sample upper end until the measured P_p reaches a stable negative value, (2) the fluid is injected at the sample bottom while maintaining the vacuum up to full saturation, and (3) the sample is flushed again by a full volume of fluid, i.e., equal to the system "sample + dead volume" total volume. Water saturation is then obtained by directly injecting water in the glycerin-filled sample. As glycerin immediately and fully dissolves in water, thus losing its viscosity, the water full saturation is obtained by flushing two to three times the pore volume.

Pore fluid setup

Pore pressure is controlled externally, and independently of the confining pressure, by a pair of connected Quizix volumetric servopumps. The pore volume and pressure measurements' accuracies are of approximately $V_p \sim 0.1$ µL and $P_p \sim 0.001$ MPa, respectively. Additionally, another pressure transducer of $P_p \sim 0.01$ MPa accuracy is placed near the sample. Valves are placed at both ends of the sample (Figure 2a) to decrease as much as possible the pipes' dead volumes (i.e., 1 and 2 in Figure 2a), and the pressure sensor is placed near the bottom endplaten (i.e., inside the dead volume). The measured dead volumes are $V_{d1} = 3.433$ mL and $V_{d2} = 3.205$ mL, leading to a total dead volume of approximately $V_d \sim 6.6$ mL.

The valves can either be open or closed. The first configuration is chosen when changing the confining pressure in the range of $P_c \in [1; 50]$ MPa, so that the fluid is kept at a constant pressure of $P_p \sim 2$ MPa. The second configuration is chosen, and the valves are closed, during LF measurements, i.e., during the small pressure oscillation ΔP_c. In this configuration, the fluid mass is kept constant in the system (i.e., sample + dead volume). This system is experimentally undrained, and fluid pressure changes are tracked by the pore-pressure sensor.

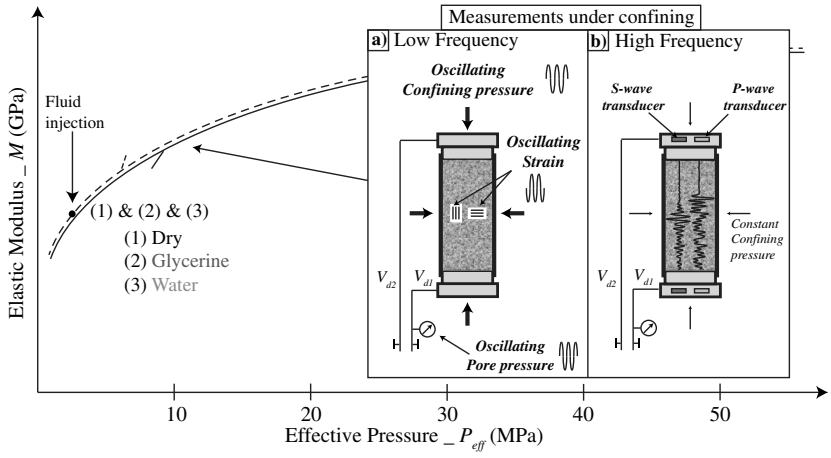

Figure 2. Schematic view of the experimental procedure. Under isotropic stress conditions, (a) LF measurements originate from a confining pressure oscillation that induces the strain and pore pressure oscillations and (b) K_{HF} is obtained from ultrasonic wave velocity measurement, from a traveling pulse between two piezoelectric transducers.

This configuration was found to be the most appropriate because it discards any possible bias from an extrinsically induced differed fluid flow (i.e., from the slow regulation of the pump). This configuration has often been chosen for measuring frequency effects (e.g., Batzle et al., 2006; Tisato and Madonna, 2012; Madonna and Tisato, 2013; Mikhaltsevitch et al., 2014). In such a setup, one would assume that the resulting measurement is intrinsically undrained. This is actually not the case here owing to the existence of the dead volume (i.e., $V_d \sim 6.6$ mL). In particular, V_d is close to the samples' total pore volumes V_p (i.e., $V_{\text{Fo7}} \sim 7.2$ mL and $V_{\text{Fo9}} \sim 8.6$ mL). It follows that $V_p + V_d$ is undrained, but V_p is not necessarily undrained.

High-frequency setup

HF moduli are measured from the traveltime of an ultrasonic wave through the sample's length (i.e., $l \sim 80$ mm). For this purpose, a pair of P- and S-wave piezoelectric transducers (PZT5A, Boston Piezo-Optics, Inc.) are glued in the end-platens, at both ends of the sample. The recorded traveltime is directly corrected from the added traveltime in the end-platens.

P- and S-wave arrival times Δt are obtained using a crosscorrelation procedure by picking the arrival-time of the P- or S-waveform's maximum amplitudes. The waves' velocities i.e., V are then inferred knowing the sample length l such that $V = l/\Delta t$. HF moduli K_{HF} and G_{HF} are obtained from the sample's density ρ and the measured P- and S-wave velocities assuming the material isotropic such that

$$\begin{cases} V_{\text{P}} = \sqrt{\frac{K_{\text{HF}} + \frac{4}{3}G_{\text{HF}}}{\rho}}, \\ V_{\text{S}} = \sqrt{\frac{G_{\text{HF}}}{\rho}}, \end{cases} \tag{1}$$

with the density ρ defined from the known quartz (i.e., ρ_{qtz}) and fluid (i.e., ρ_f) densities, and sample's porosity (i.e., ϕ) such that $\rho = \rho_f.\phi + \rho_{\text{qtz}}.(1 - \phi)$.

Note that the sample's length varies with the confining pressure. A length correction $l = l_0 - \Delta l$ is thus introduced in the measurement of the wave velocities. In the same way, the sample density varies due to the porosity change $\phi = \phi_0 - \Delta\phi$ so that a second correction is also introduced to obtain the HF elastic moduli (e.g., K_{HF}).

The relative elastic waves velocities values obtained from crosscorrelation measurements have accuracies of 0.1%. However, owing to the uncertainty to precisely determine the arrival time on the reference waveforms, absolute P- and S-wave velocities have lower accuracy, of approximately 1% and 3%, respectively. Because the aim of the present contribution is to compare HF and LF moduli, and not the sole effect of the fluid on the P- and S-wave velocities, absolute measurements are needed. Because the elastic moduli are deduced from the square of the ultrasonic wave velocities, they bear a much larger measurement error. G_{HF} is inferred from V_{S} only. The low accuracy on the V_{S} only affects its absolute value, with an accuracy as low as 6%. On the reverse, K_{HF} is inferred from a combination of V_{P} and V_{S}. The absolute accuracy on K_{HF} is thus lower than for G_{HF}, i.e., accounting for errors on P- and S-wave velocities. Its error is assumed to be higher than approximately 8%.

Low-frequency setup

As discussed above, the LF measurements rely on the stress-strain method. A low-amplitude pressure oscillation at a given frequency is applied on the sample, thus inducing a strain oscillation. Three pairs of axial and radial 350Ω strain gauges (Tokyo Sokki TML, FCB-6-350-11) of 6-mm length are directly glued on the sample. Each of the six strain gauges are mounted in a one-fourth Wheatstone bridge. Pressure ΔP_c and strain $\Delta\epsilon$ oscillations are transformed from electric to pressure and strain signals using the Catman recording system (HBM, Inc.), able to record at frequencies up to 2400 Hz.

Two different approaches are used for the sample's investigation. First, properties are measured as a function of effective pressure, at a chosen frequency of $f \sim 0.1$ Hz. Second, properties are measured as a function of frequencies at various confining pressures.

Processing method for the low-frequency setup

At a given effective pressure, an oscillating confining pressure ΔP_c (Figure 3a) leads to strain $\Delta\epsilon$ oscillations (Figure 3c), and, in the case of porous samples saturated by a liquid, to a pore pressure ΔP_p oscillation (Figure 3b). The recorded strains account for a solid response to the applied pressure oscillation. The pore-pressure oscillations, recorded at the outlet of the pipes' dead volume, account for a fluid response induced by the sample's response.

The applied confining pressure oscillations ΔP_c (Figure 3a) are triangular periodic signals. As a direct consequence, the output registered signals for strain $\Delta\epsilon_v$ (Figure 3c) and pore pressure ΔP_p (Figure 3b) have the same triangular form. The signal is a periodic function characterized by its frequency f, phase ϕ, and amplitude A.

Volumetric strain measurement

As Madonna and Tisato (2013) point out, the sample intrinsic heterogeneity may induce an error because the total rock volumetric strain may differ from the local strain recorded by the gauge. To discard such error (1) the samples (i.e., reference and Fontainebleau samples) used have been chosen to be homogeneous media, and (2) large strain gauges (i.e., 6-mm length) have been used so that the measurement area is larger than an REV average area.

The volumetric strain ϵ_v is theoretically obtained from axial ϵ_{ax} and radial ϵ_{rad} strains such that $\epsilon_v = \epsilon_{\text{ax}} + 2\epsilon_{\text{rad}}$. However, under pure isotropic conditions, the measured ϵ_{ax} and ϵ_{rad} are equal (e.g., Figure 3c). It is thus possible to deduce ϵ_v either from ϵ_{ax} (David et al., 2013) or ϵ_{rad} only. To minimize the possible bias, the volumetric strain is here measured from the mean of all gauges so that $\epsilon_v = 3.\bar{\epsilon}$, where $\bar{\epsilon}$ is the mean value of all the strain gauges (i.e., ϵ_{ax} and ϵ_{rad}).

Strain measurement

In an automatic procedure, (1) the signals (e.g., Figure 3) are Fourier transformed; (2) the frequency f, corresponding to the dominant amplitude peak A, is picked; and (3) the phase ϕ, corresponding to the picked frequency f, is in turn picked. The bulk phase shift $\Delta\phi_K$ is obtained from the phase difference between stress and strain (Batzle et al., 2006; Madonna and Tisato, 2013), such that the bulk attenuation $Q_K^{-1} = \tan[\Delta\phi_K]$ is obtained.

During the experiment, the air conditioning of the experimental room results in an extrinsic oscillation (Figure 3) of low frequency

(i.e., $f \sim 10^{-3}$ Hz). The recorded signal is then filtered in the Fourier domain to suppress this noise. As shown for the gypsum sample (Figure 4a), after filtering, stress and strain oscillations have the same frequency f. Because strain is negative in compression, stress and strain are in phase opposition.

Under purely isotropic conditions, the LF bulk modulus K_{LF} is obtained from measured stress ΔP_c and strain $\Delta\epsilon_v$ such that $\Delta P_c = K_{LF} \times \Delta\epsilon_v$. The K_{LF} is obtained by a linear regression constrained with a 99% confidence interval. The data scatter around this linear regression is used to infer a statistical error, noted ΔK_{LF}. An example is reported (Figure 4b) for the three standard samples measured under the same conditions of (1) a low confining pressure (i.e., $P_c = 1$ MPa) and (2) an oscillating pressure of $\Delta P_c = 0.2$ MPa at a frequency of 0.1 Hz. Because the signal-to-noise ratio decreases when the strain amplitude decreases, thus decreasing the strain gauge accuracy, the error is larger for the stiffer glass and gypsum than for the soft Plexiglas. Yet, this statistical error remains lower than approximately 1% of the measured modulus.

Pore-pressure measurement

Again, the temperature oscillation is filtered to obtain the pore pressure oscillations measurements. An example is shown (Figure 5) for Fo9 fully saturated by either water or glycerin. Pore pressure oscillations (i.e., ΔP_p) can be measured (Figure 5a) for a given effective pressure and frequency.

From ΔP_p measurements under purely isotropic oscillations, it is possible to obtain a pseudo-Skempton coefficient B^* of our undrained system (i.e., sample + dead volume) such that $\Delta P_p = B^* \times \Delta P_c$. Because the undrained volume corresponds to $V_p + V_d$, and not V_p only, this coefficient B^* may not equal B. Using a linear regression, with a 99% confidence interval, B^* is obtained (Figure 5b). It is clear from Figure 5b that an hysteresis is present. This means that there is a phase shift between ΔP_c and ΔP_p. The data scatter around this linear regression, noted ΔB^*, is in fact directly related to this phase shift.

Measuring pore-pressure oscillation at the outlet of the dead volume implies that the overpressure caused in the poral fluid by the oscillation induces a fluid flow out of the sample. In other words,

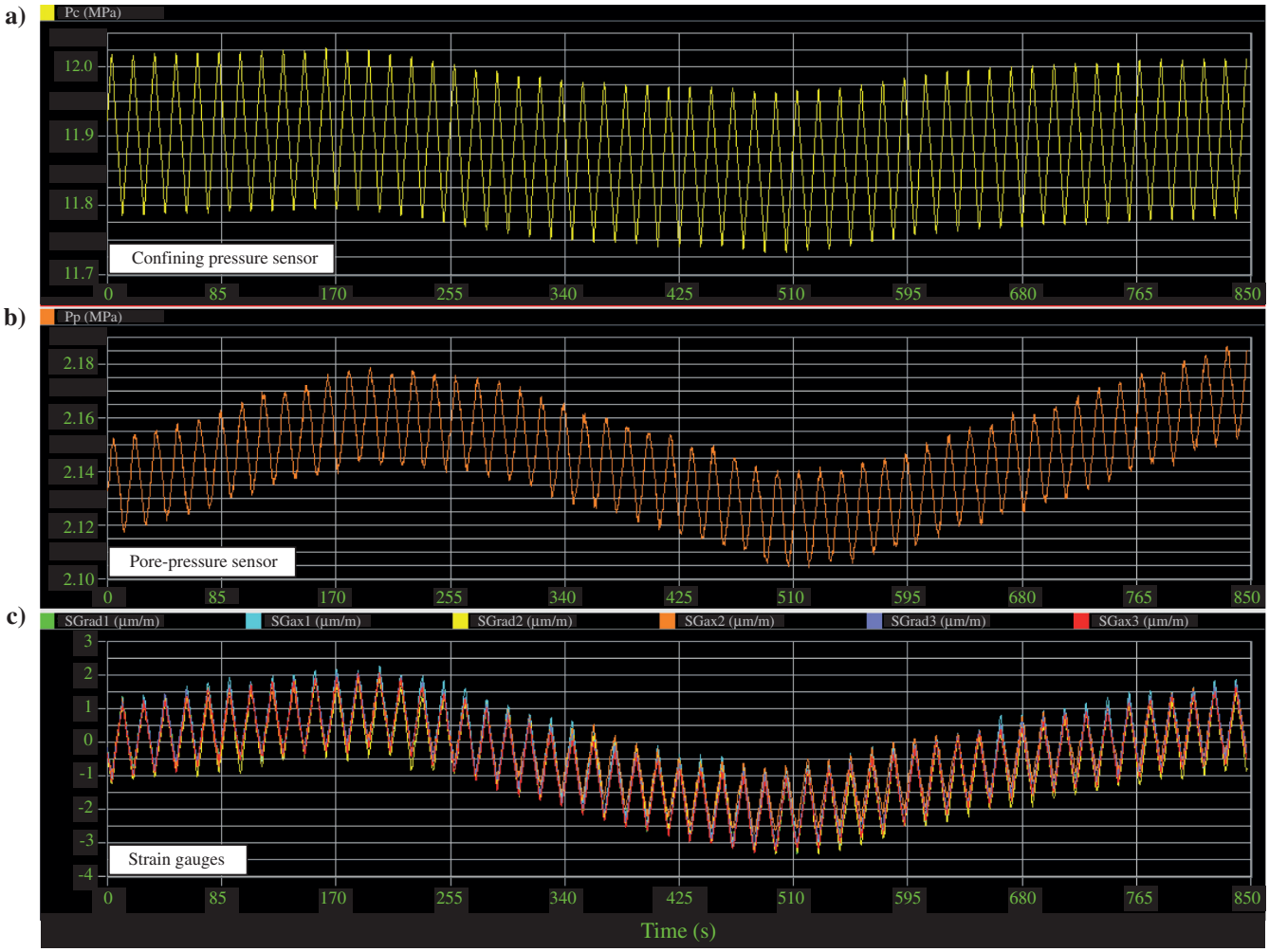

Figure 3. Recorded measurement of (a) confining pressure oscillations ΔP_c, (b) induced pore pressure ΔP_p, and (c) axial and radial strains $\Delta\epsilon_{rad}$ and $\Delta\epsilon_{ax}$ oscillations prior to signal processing. Snapshot for Fo7 under glycerin saturation at an effective pressure of 10 MPa (i.e., $P_c = 12$ MPa and $P_p = 2$ MPa) is taken. For this example, the signal frequency is $f = 0.06$ Hz and the sampling frequency is $f = 0.5$ Hz. Note the LF modulation due to the air-conditioning system.

the ΔP_p oscillations are induced by a fluid flow out of the sample. Conversely, if no fluid pressure oscillations ΔP_p are observed, the implication is that there is no time for fluid to flow out of the sample into the dead volume; i.e., the sample is undrained. Note that, for same effective pressure (i.e., $P_{\text{eff}} \sim 1$ MPa) and oscillating frequency (i.e., $f \sim 0.1$ Hz), the pore pressure response shows a dependence to the saturating fluid in case of Fo9 (Figure 5b). This difference exists for B^* and ΔB^*. It implies that, under the same measuring conditions, less fluid flow is allowed in the case of glycerin saturation and that the phase shift is larger. This is consistent with a higher viscosity value for glycerin as compared to water.

CALIBRATION RESULTS

The detailed procedure and processing methods are first tested on the three reference/standard samples to assess the behaviors of apparatus and oscillating system, and thus the accuracy of the reported measurements.

Limitations of the apparatus

The oscillating system is first tested to determine the range of pressure values that give reliable data. In particular, one needs to check that strain amplitudes are low enough to avoid inelastic effects. As discussed by Winkler and Murphy III (1995), dependence of elastic properties on amplitude could be observed even at strain amplitudes as low as $\Delta\epsilon \sim 10^{-6}$ (Winkler, 1985). Yet, these inelastic effects prove to be negligible (i.e., less than approximately ~1%) for strain amplitudes lower than approximately $\Delta\epsilon \sim 10^{-5}$ (see Figure 6 from Winkler and Murphy III, 1995).

Using plots of $\Delta P_c - f$ (Figure 6a) and $\Delta\epsilon_v - f$ (Figure 6b), the domain in which the apparatus is reliable can be constrained. For this apparatus, ΔP_c amplitudes (Figure 6a) originate from pump piston oscillations and thus directly correlate with the frequency of oscillation. Because measurements prove not to be accurate for strain variations lower than approximately $\Delta\epsilon \sim 3.10^{-7}$ (Figure 6b), measuring frequencies higher than approximately $f \sim 1$ Hz is out of the reliable range. The domain at which inelastic effects are present is also discarded (Figure 6b).

Strains of $\Delta\epsilon \sim 1 - 3.10^{-6}$ have been chosen for the measurements at each confining pressure for all samples. Note that the strains measured in the samples can be predicted knowing their bulk modulus. Sandstones' bulk moduli range between approximately $K \sim 10$ GPa and $K_s \sim 38$ GPa, so that from Figure 6, the maximum frequency is $f \sim 0.4$ Hz. Owing to these limitations (Figure 6), the frequency range of interest for the reported experiment on Fontainebleau sandstone samples is $f \in [4.10^{-3}; 4.10^{-1}]$ Hz.

Confining pressure effect for the reference samples

As discussed in the experimental procedure, K_{LF} and K_{HF} have been measured simultaneously at each confining pressure step start-

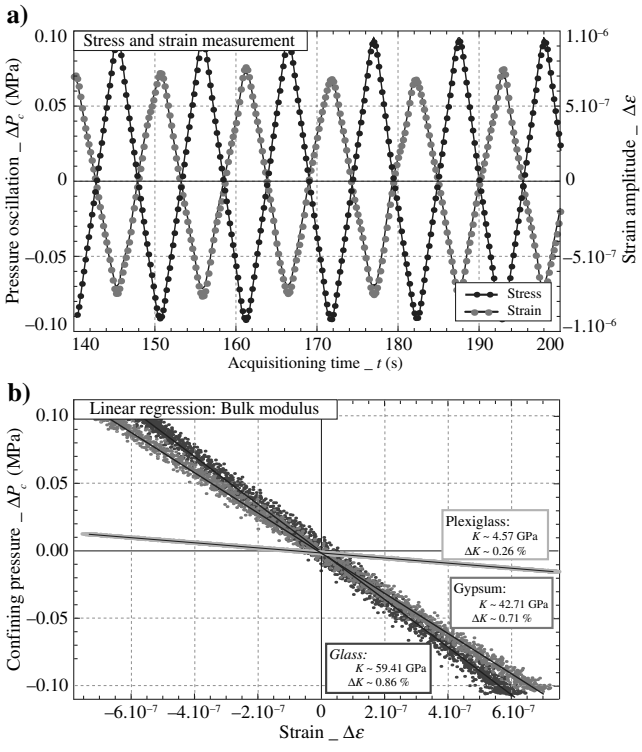

Figure 4. Example of stress-induced strain oscillations at a frequency of $f = 0.1$ Hz and a confining pressure of $P_c = 1$ MPa: (a) stress (i.e., black) and induced strain (i.e., gray) oscillations for the gypsum sample and (b) linear regressions for the three standard samples. The ΔK_{LF} values correspond to the statistical error on the measured K_{LF}.

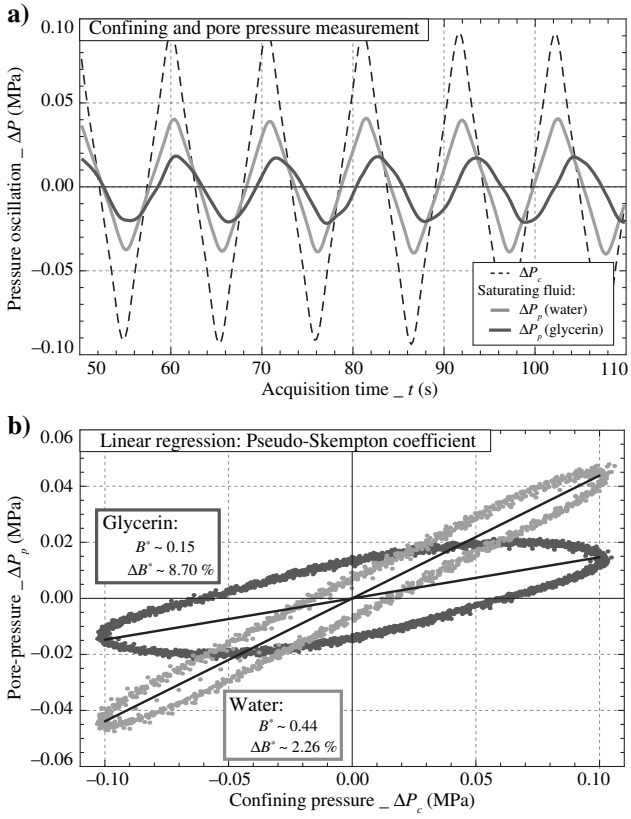

Figure 5. Example of stress-induced pore-pressure oscillations at $f = 0.1$ Hz and $P_{\text{eff}} = 1$ MPa for the water- and glycerin-saturated Fo9: (a) confining (i.e., black) and induced pore (i.e., gray) pressure oscillations and (b) linear regressions for the water (i.e., light gray) or glycerin (i.e., dark gray) saturations.

ing from $P_c = 1$ MPa up to $P_c = 50$ MPa. The measurements at frequencies of $f \sim 0.1$ Hz and $f \sim 0.5$ MHz are reported (Figure 7a) as a function of confining pressure. No pressure variation is observed for all three standards (i.e., glass, gypsum, and Plexiglas). This shows that LF and HF measurements are reliable at all pressures. Furthermore, K_{LF} and K_{HF} have the same values, which are the ones known for these standard samples.

Attenuation has also been measured from the LF periodic signal (Figure 7b). For all confining pressures, values of $Q_K^{-1} \sim 0.02$ are found for the PMMA, and values of $Q_K^{-1} \sim 0.01$ are found for the glass and gypsum samples. The larger value of the PMMA is consistent with the viscoelastic dispersive properties of this material (e.g., Batzle et al., 2006). Overall, the measurements indicate that the apparatus is able to detect variations as small as $Q_K^{-1} \sim 0.01$.

Frequency effect for the reference samples

For a chosen confining pressure, the standard samples have been measured at the different frequencies in the range allowed by the apparatus (i.e., $f \in [4.10^{-3}; 4.10^{-1}]$ Hz). Because K_{LF} largely differs from one sample to the other (Figure 7), the values are normalized to evidence a possible frequency effect (i.e., dispersion). The K_{LF} at the lowest frequencies K_0 is thus chosen as a reference to define a dispersion coefficient DispK_{LF} such that

$$\text{Disp}\, K_{LF} = \frac{K_{LF} - K_0}{K_0}. \quad (2)$$

The frequency dependence of DispK_{LF} (Figure 8a) and Q_K^{-1} (Figure 8b) is presented for the three standard samples, for a fixed confining pressure of 1 MPa. Although no variation is observed for glass and gypsum samples, Plexiglas DispK_{LF} values appear to increase with frequency. This evolution directly correlates to a peak in attenuation of $Q_K^{-1} \sim 0.04$. All measurements result consistent because (1) glass and gypsum are purely elastic media in the investigated pressure and frequency range and (2) Plexiglas is known to be a viscoelastic solid (e.g., Batzle et al., 2006).

Note that, in the case of the Plexiglas sample, the measured dispersion (i.e., Disp$K_{LF} \sim 9\%$) is a small effect that corresponds to an increase in bulk modulus from 4.32 up to 4.71 GPa at highest frequencies. It implies that the apparatus allows for measurement of effects as small as the one presented here.

RESULTS ON FONTAINEBLEAU SANDSTONE

Experiments similar to those described for the three standard samples were performed on the two Fontainebleau sandstone samples. These samples are porous, and the measurements were performed at full saturation (i.e., dry, water, and glycerin).

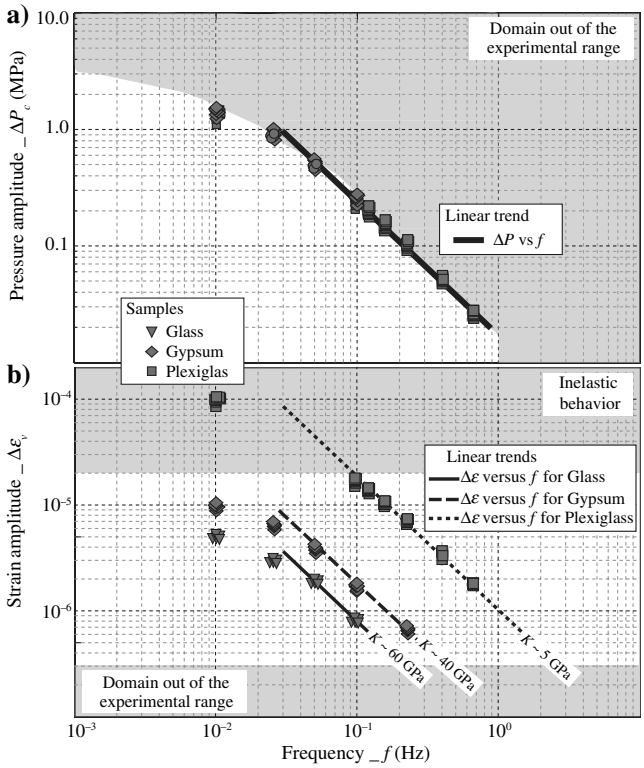

Figure 6. Measurement of (a) stress and (b) strain amplitudes for a given frequency. Symbols correspond to measurements on glass (i.e., triangles), gypsum (i.e., diamonds), and Plexiglas (i.e., squares). In panel (a), the gray zone corresponds to a domain out of the experimental range. In panel (b), the upper gray area corresponds to the inelastic behavior and the lower gray area corresponds to a domain out of the experimental range.

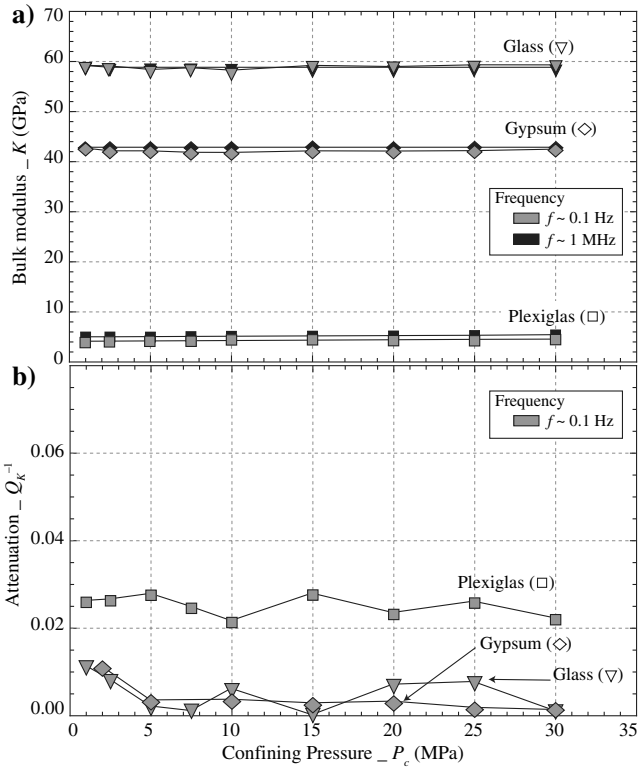

Figure 7. Measured (a) bulk modulus and (b) attenuation on three reference samples for different confining pressures. LF and HF (i.e., $f = 0.1$ Hz, i.e., $f \sim 0.5$ MHz) are represented in gray and black, respectively, for the samples of glass (i.e., triangles), gypsum (i.e., diamonds), and Plexiglas (i.e., squares).

Pressure dependence of the samples' elastic properties

The HF bulk modulus K_{HF}, inferred from V_P and V_S, is reported (Figure 9a and 9b) as a function of P_{eff}. Under dry conditions, both samples show a pressure-dependent increase in K_{HF}. Yet the magnitude in variation is much higher in Fo7, starting from ~14 GPa at lowest confining up to ~33 GPa at 50 MPa. Under water and glycerin saturation, however, a small decrease in K_{HF} is inferred for an increase in effective pressure. This small decrease remains smaller than the error of measurement, so that we may consider the K_{HF} of these fluid-saturated samples to be constant with pressure.

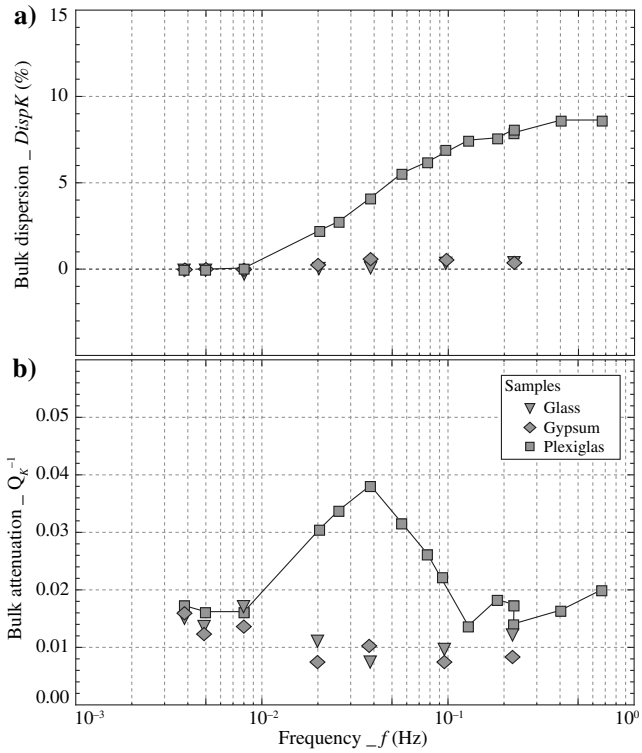

Figure 8. Measured (a) bulk modulus and (b) attenuation on the three reference samples as a function of the oscillation frequency for a confining pressure of $P_c \sim 1$ MPa.

LF bulk modulus K_{LF} and attenuation Q_K^{-1} were obtained from pressure oscillations ΔP_c at $f \sim 0.1$ Hz following the same protocol as above. For both rocks, the measured K_{LF} (Figure 10a and 10b) and Q_K^{-1} (Figure 10c and 10d) are reported as a function of effective pressure. Overall, one observes a clear dependence to the effective pressure and the fluid nature. Both samples show very similar behaviors. Under dry conditions, the measured K_{LF} (Figure 10a and 10b) and K_{HF} (Figure 9a and 9b) have similar values and follow the same pressure dependence in the range of $P_{eff} \in [1 - 50]$ MPa. A larger pressure dependence is measured in Fo7. Beyond $P_{eff} \sim 10$ MPa, the pressure dependence is negligible for Fo9 and very small for Fo7.

In fluid-saturated conditions, K_{LF} (Figure 10a and 10b) and K_{HF} (Figure 9a and 9b) have different values. For glycerin and water saturations, K_{HF} values are higher and almost not fluid or pressure dependent. Oppositely, K_{LF} varies with effective pressure and its values are different in water- or glycerin-saturated conditions. The difference between dry and water-saturated LF values is very small. In the glycerin-saturated case, the K_{LF} value is higher. Beyond 10 MPa, the pressure dependence is negligible for Fo9 and very small for Fo7.

The K_{LF} plots (Figure 10a and 10b) tightly correlate with the attenuation Q_K^{-1} plots (Figure 10c and 10d). In particular, no attenuation is observed for dry and water-saturated conditions, and a large increase in attenuation under glycerin saturation is observed at low effective pressures (i.e., $P_{eff} < 10$ MPa).

Frequency dependence in the low-frequency range at 1 MPa

At a fixed pressure (i.e., $P_{eff} \sim 1$ MPa), K_{LF}, Q_K^{-1}, and B^* have been measured over the frequency range of $f \in [4.10^{-3}; 4.10^{-1}]$ Hz allowed by the apparatus (Figure 6).

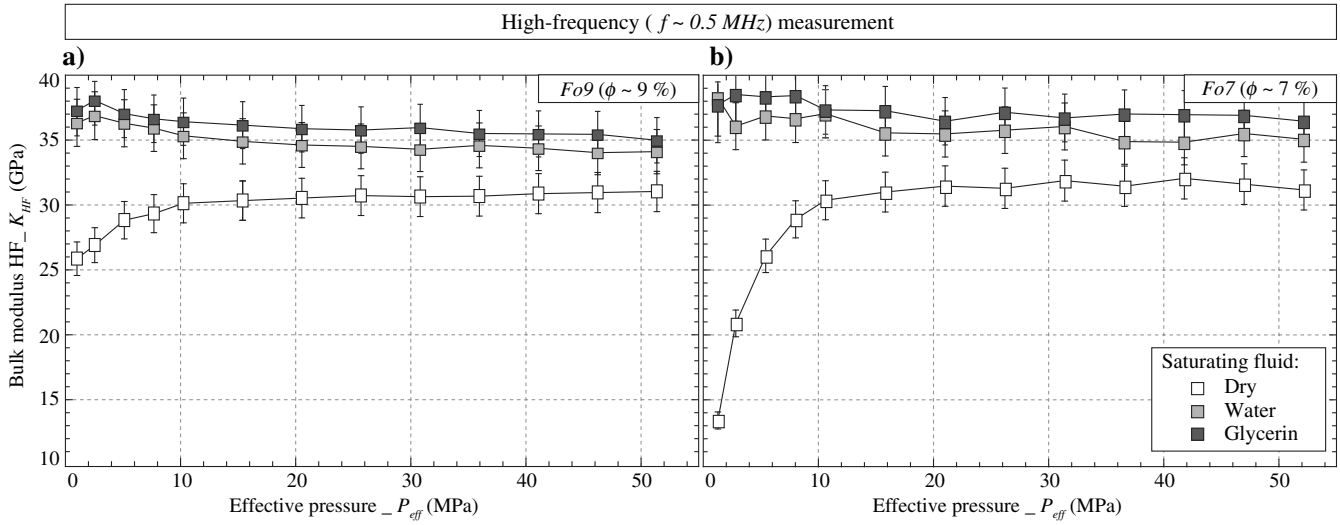

Figure 9. Measurement of the pressure dependence of Fo9's and Fo7's HF bulk moduli (K_{HF}). The K_{HF} is measured for the three different saturating fluids and effective pressures up to approximately $P_{eff} \sim 50$ MPa.

Strain measurement: K_{LF} and Q_K^{-1}

For both samples, the effects of the different fluids' full saturation on the LF bulk moduli K_{LF} (Figure 11a and 11b) and attenuations Q_K^{-1} (Figure 11c and 11d) are compared. As in the pressure dependence study (Figure 10), measurements under glycerin saturation differ from the ones under dry or water-saturated conditions.

Almost no frequency dependence is observed on K_{LF} (Figure 11a and 11b) under dry and water-saturated conditions, and the Fo7 (i.e., $K_{LF} \sim 14$ GPa) and Fo9 (i.e., $K_{LF} \sim 25$ GPa) values are constant. Oppositely, a large frequency dependence is observed for the glycerin-saturated samples. In this last case, K_{LF} increases with frequency up to a value of 34 GPa for Fo9 and 26 GPa for Fo7 at $f \sim 4.10^{-1}$ Hz.

These results correlate well with Q_K^{-1} data (Figure 11c and 11d). The measured Q_K^{-1} show very low values and almost no variation under dry or water-saturated conditions. Oppositely, a large frequency-dependent variation is observed under glycerin saturation. For this case, an attenuation peak of $Q_K^{-1} \sim 0.15$ and $Q_K^{-1} \sim 0.25$ is observed for Fo9 and Fo7, respectively, at intermediate frequencies.

Pore-pressure variations

The frequency dependence of B^* is reported (Figure 12a and 12b) for the water- and glycerin-saturated conditions. For both samples, the measured B^* values under water saturation differ from the ones under glycerin-saturated conditions. In the water-saturated case, B^* is almost constant for both samples. In the glycerin-saturated case, the B^* values show a large decrease with frequency, down to approximately 0 at higher frequencies.

Under water-saturated conditions, the pressure oscillations are observed for all frequencies in the dead volume. It implies that a fluid flow in and out of the sample occurs under water saturation whatever the frequency is. Under glycerin-saturated conditions, while the pressure oscillations are observed in the dead volume at lower frequencies, no oscillations are transmitted to the dead volume as f approaches 0.4 Hz. In agreement with that observation, one notes that, for both rocks, the frequency-dependent variations in B^* (Figure 12) directly correlate with the independently measured increase in K_{LF} (Figure 11) in both glycerin-saturated samples. It implies that fluid is less and less squeezed out from the sample to the pipes' volume as the frequency increases, up to a frequency for which no fluid is allowed to flow out of the

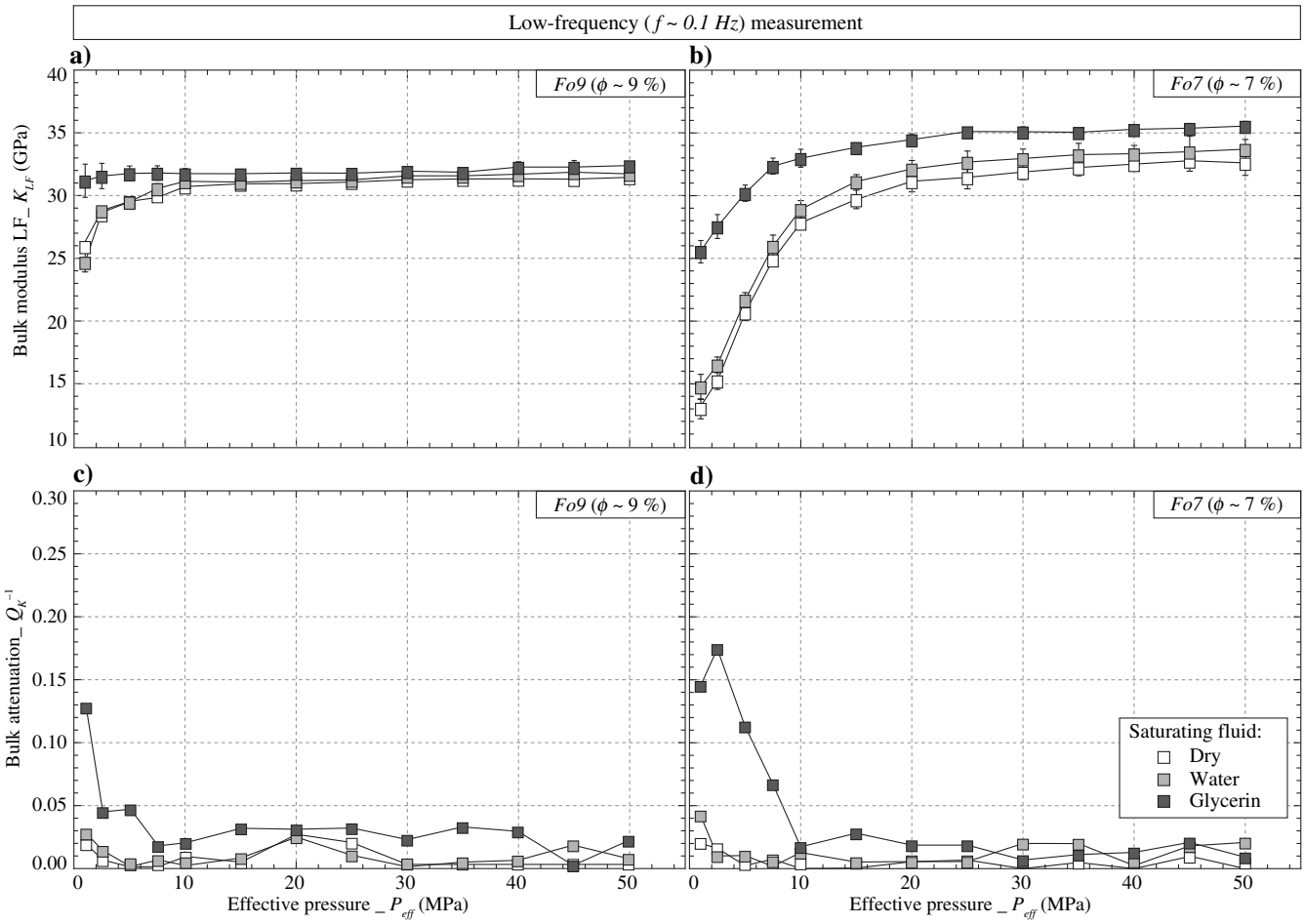

Figure 10. Measurement of the pressure dependence of Fo9 and Fo7 LF elastic properties. For both samples, (a and b) the LF bulk moduli K_{LF} and (c and d) attenuation Q_K^{-1} are measured for the three different saturating fluids for effective pressures up to approximately $P_{eff} \sim 50$ MPa.

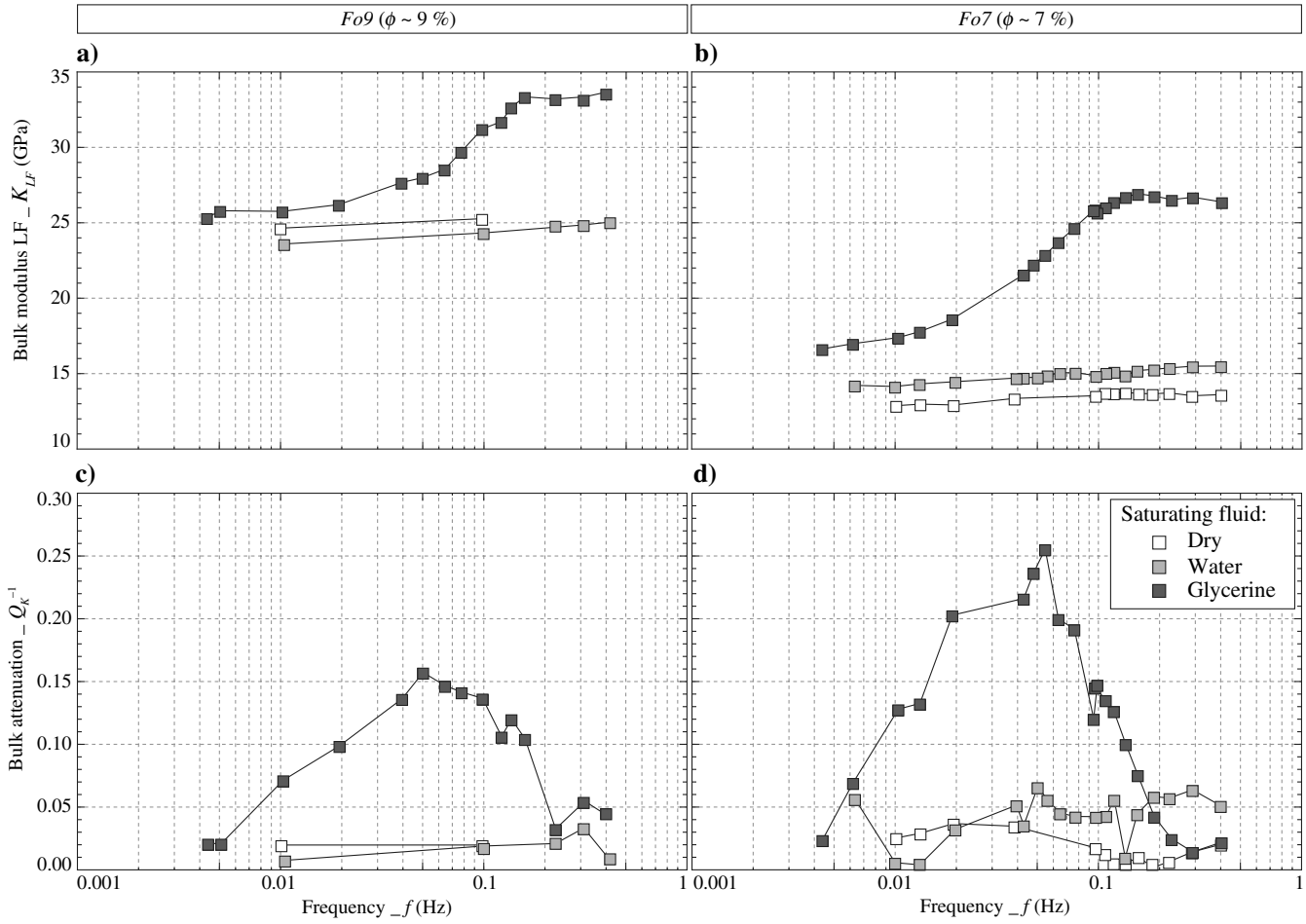

Figure 11. Measurement of the frequency dependence of Fo9 and Fo7 elastic properties at $P_{\text{eff}} \sim 1$ MPa. For both samples, (a and b) the bulk modulus K_{LF} and (c and d) attenuation Q_K^{-1} are measured for the three different saturating fluids in the frequency range of $f \in [4.10^{-3}; 4.10^{-1}]$ Hz.

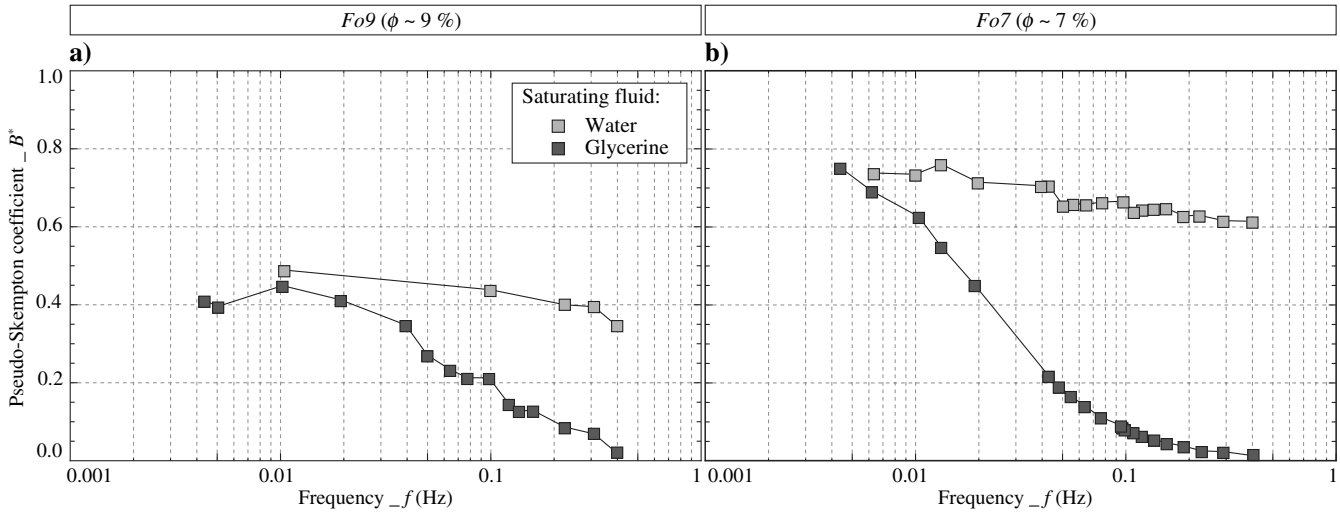

Figure 12. Measurement at $P_{\text{eff}} \sim 1$ MPa of the frequency dependence of the pseudo-Skempton coefficients B^* in (a) Fo9 and (b) Fo7 saturated by either water or glycerin.

sample. In other words, the samples are undrained at these higher frequencies.

Frequency dependence in the low-frequency range at four effective pressures

The measurements have been done for Fo7 for which the frequency dependence has been found to be the largest (Figures 11 and 12). The frequency-dependent properties are measured for $P_{\text{eff}} = [1; 2.5; 10; 30]$ MPa.

Strain measurements: K_{LF} and Q_K^{-1}

A strong pressure dependence is measured for the water-saturated K_{LF} (Figure 13a). Again, no frequency dependence is observed. At low frequencies, all glycerin-saturated K_{LF} (Figure 13b) have values close to the water-saturated ones. Increasing the frequency leads to an increase in the glycerin-saturated K_{LF} values. This frequency dependence is largely damped by the increase in effective pressure. However, at all effective pressures, the variation takes place in the same frequency range.

Again, the measured frequency dependences of K_{LF} and Q_K^{-1} show a good correlation. The water-saturated Q_K^{-1} (Figure 13c) is low (<0.05) for all effective pressures. Under glycerin saturation (Figure 13d), a large frequency-dependent attenuation peak is measured. Increasing the effective pressure results in a clear Q_K^{-1} decrease.

Pore pressure variations

For water- and glycerin-saturated conditions, a large decrease in B^* (Figure 14a and 14b) is measured when increasing effective pressure. As for the measured K_{LF}, for a given effective pressure, B^* values measured under glycerin saturation at lowest frequency are close to the water-saturated (Figure 14a) ones. Only in the glycerin-saturated case (Figure 14b), B^* shows a large decrease with frequency. This frequency dependence decreases with increasing effective pressure because the magnitude of B^* decreases.

Comparing the measured K_{LF} (Figure 13a and 13b) and B^* (Figure 14a and 14b) shows a direct correlation between the frequency and pressure dependence. The observed pressure and frequency dependence of B^* correspond to a decreasing fluid flow out of the sample with increasing frequency and effective pressure.

INTERPRETATION

Rock-physics framework

Dispersion and attenuation effects in porous rocks have been discussed by Cleary (1978) in terms of three fluid-flow regimes

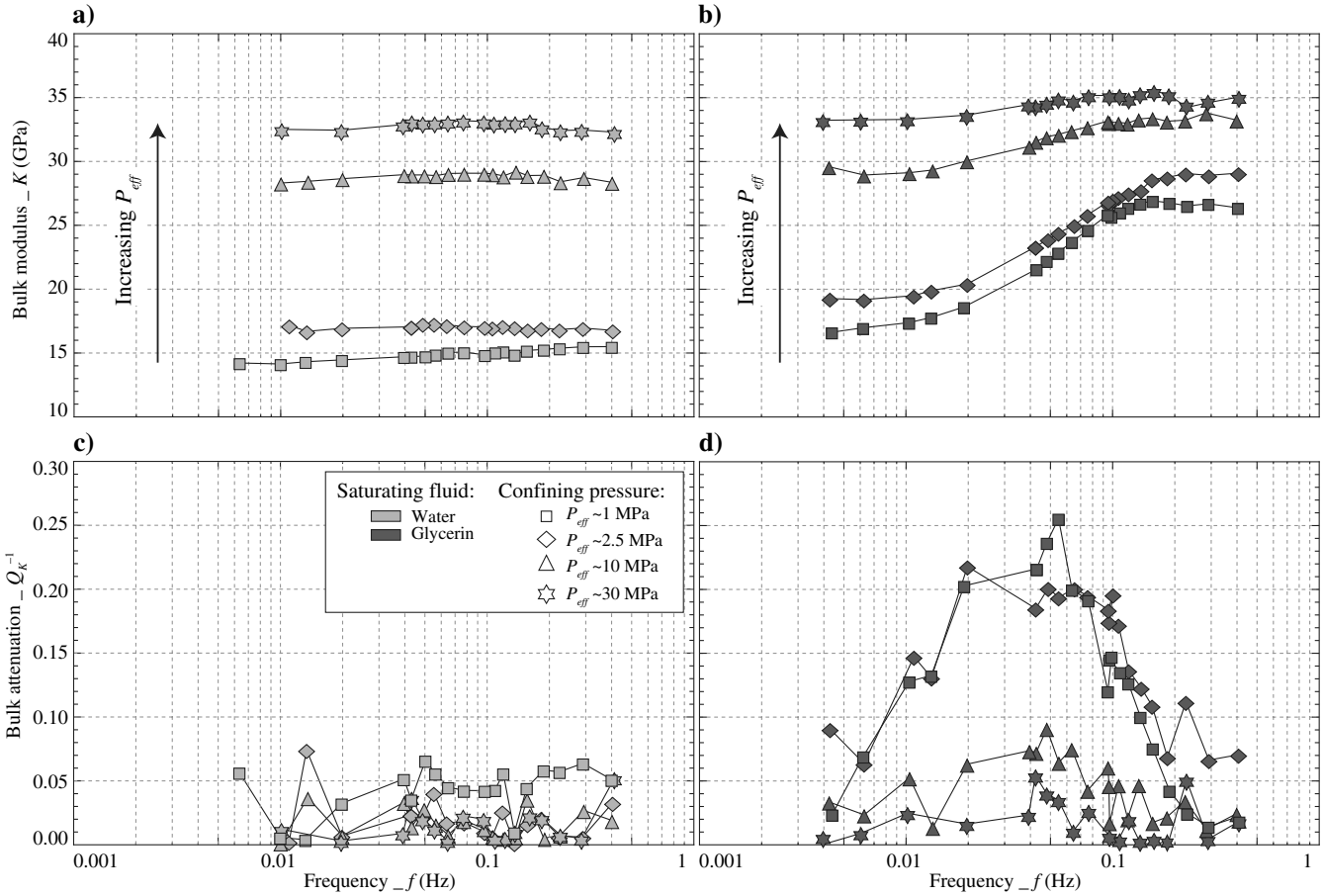

Figure 13. Measurement of the frequency dependence of Fo7 elastic properties under water or glycerin saturations for four different confining pressures. (a and b) LF bulk modulus K_{LF} and (c and d) attenuation Q_K^{-1} are measured at the different frequencies allowed by the apparatus for the three different fluids.

(Figure 15a). The transitions between these flow regimes are characterized by two critical frequencies, which values depend on the specific rock/fluid system (Sarout, 2012). Using Zener viscoelastic model (e.g., Nowick and Berry, 1972), the K and Q_K^{-1} expected behaviors for these two transitions are summarized in Figure 15b.

At LFs, following Cleary (1978), one can expect to observe the drained and undrained regimes of quasistatic poroelasticity (Gassmann, 1951). The Biot-Gassmann equation relates the undrained elastic modulus K_u to the drained bulk modulus K_d, the sample porosity ϕ, the fluid bulk modulus K_f, and the skeleton (i.e., quartz in our case) bulk modulus K_s such that (Gassmann, 1951):

$$K_u = K_d + \frac{\alpha^2 K_f}{\phi + (\alpha - \phi)\frac{K_f}{K_s}}, \tag{3}$$

where α is the Biot coefficient, defined as $\alpha = 1 - (K_d/K_s)$.

The drained regime is that of a macroscopic fluid flow. Typically, that means a fluid flow over one wavelength at the field scale. Because at low frequencies the wavelength is large (i.e., a few kilometers at 1 Hz) and the rock permeability is low, seismic waves cannot "see" this regime. At the laboratory scale, however, the forced oscillations mode can correspond to a drained regime because the sample length L is much smaller than the wavelength λ. As discussed by Cleary (1978), the time constant for fluid flow over the sample length L depends on the hydraulic diffusivity d such that

$$d = K_d \frac{k}{\eta}, \tag{4}$$

where k is the rock permeability, and η is the fluid viscosity. It results that the critical frequency for the drained/undrained transition is $f_1 = d/(L/2)^2$ or

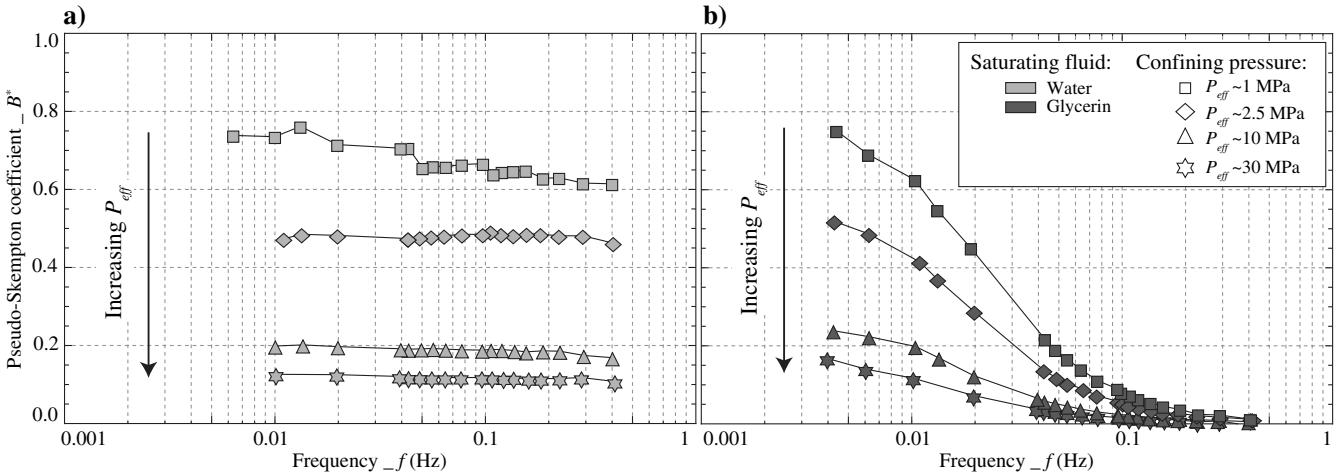

Figure 14. Measurement of the frequency dependence of the pseudo-Skempton coefficients B^* in Fo7 saturated by either (a) water or (b) glycerin for four different effective confining pressures.

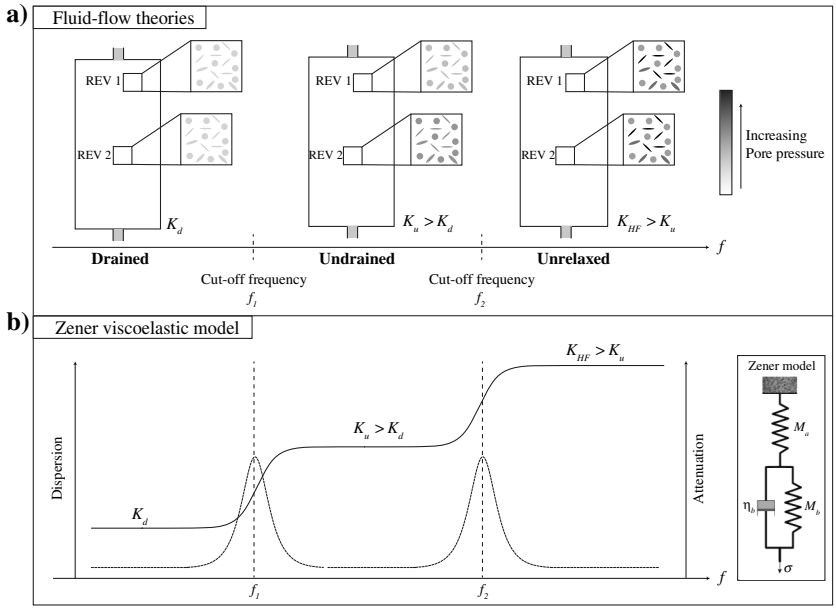

Figure 15. (a) Schematic view of the three elastic regimes for a fully saturated rock: drained, undrained, and unrelaxed. Each transition between two regimes corresponds to a critical frequency f. (b) Schematic representation of the dispersion and attenuation expected from a fluid-flow mechanism among the drained, undrained, and unrelaxed domains.

$$f_1 = \frac{4kK_d}{\eta L^2}. \quad (5)$$

At higher frequencies, poroelasticity may not be applicable. This will be the case if the REV is not isobaric; i.e., the fluid has not enough time to reach an isobaric state within a REV. In that case, a third flow regime is present that is called *unrelaxed*. Because, in general, a porous rock contains inclusions of different shapes (i.e., pores and microcracks), fluid can flow from a compliant microcrack to a neighboring less compliant pore (O'Connell and Budiansky, 1977). This squirt-flow phenomenon is associated with a critical frequency that depends on K_d, on the microcrack aspect ratio ξ and on the fluid viscosity η such that (O'Connell and Budiansky, 1977)

$$f_2 = \frac{\xi^3 K_d}{\eta}. \quad (6)$$

Note that owing to this form, f_2 depends highly on the aspect ratio ξ so that for a given fluid's viscosity, a variation in ξ of one order of magnitude would lead to a variation of three order of magnitudes in f_2. The frequency f_2 corresponds to the undrained/unrelaxed transition; i.e., f_2 cannot be lower than f_1. This is because the "relaxed" state is that in which quasistatic poroelasticity does apply; i.e., the fluid pressure is isobaric within the REV.

Interpretation of the frequency effects at 1 MPa

Accounting for fluid and frequency through the apparent frequency concept

As shown above, f_1 (Equation 5) and f_2 (Equation 6) depend on η^{-1}. The viscosity effect may thus be accounted for in the same manner as frequency (Batzle et al., 2001) by defining an apparent frequency as

$$f_f^* = f \times \frac{\eta_f}{\eta_0}, \quad (7)$$

with $\eta_0 = 10^{-3}$ Pa.s^{-1}. For the frequency range allowed by the apparatus (i.e., $f \in [4\ 10^{-3}; 4\ 10^{-1}]$ Hz), the range in apparent frequencies is (1) $f^*_{wat} \in [3.5\ 10^{-3}; 3.5\ 10^{-1}]$ Hz for the measurements under water full saturation (i.e., $\eta_{wat} = 0.890.1^{-3}$ Pa. s^{-1}) and (2) $f^*_{gly} \in [4.3\ 10^{-3}; 4.3\ 10^{2}]$ Hz for the measurements under glycerin full saturation (i.e., $\eta_{gly} = 1.087$ Pa. s^{-1}). The corresponding apparent cutoff frequencies f_1^* and f_2^* may also be defined within this framework such that

$$f_1^* = \frac{4\kappa K_d}{\eta_0 L^2} \text{ and } f_2^* = \frac{\xi^3 K_d}{\eta_0}. \quad (8)$$

Using the specific parameters values for our experiments, it is finally possible to calculate these cutoff frequencies for both rocks. The sample water permeabilities and drained bulk moduli at $P_{eff} \sim 1$ MPa are measured (Table 1). The diffusion length (i.e., $L/2$) has been chosen as equal to the sample's half-length or length (e.g., $L \sim 40$–80 mm). The aspect ratio values can be inferred from the pressure dependence of the dry moduli (Walsh, 1965). Inferred aspect ratios for Fo9 and Fo7 are approximately $\xi \sim 1$–2.10^{-4} and $\xi \sim 4$–5.10^{-4}, respectively. The resulting properties and deduced cutoff frequencies are given in Table 1.

It appears directly from Table 1 that the two samples have different apparent cutoff frequencies. Although f_1^* and f_2^* are separated by one or two orders of magnitude in the case of Fo7, they fall in a similar range for Fo9. As discussed in the following, this fact is unusual and has important consequences.

Case of Fo7 sample: A standard behavior

Measured values of K_{LF} and Q_K^{-1} at $P_{eff} \sim 1$ MPa are reported as a function of f^* (Figure 16). An increase in K_{LF} with f^* is clearly evidenced.

Considering the low f^* value of K_{LF} (i.e., ~15 GPa) to be the value for the drained modulus K_d, the Biot-Gassmann undrained prediction is $K_u = 26$ GPa. This value is very close to the measured K_{LF} at higher apparent frequencies of $f^* = 200$ Hz. The transition from drained to undrained domains is evidenced in that case. The predicted K_u and f_1^* values are consistent with the data. One can conclude that the drained/undrained transition is observed for a critical frequency of $f_1^* \sim 100$ Hz. This conclusion is further confirmed by the large attenuation peak of approximately $Q_K^{-1} \sim 0.25$ at $f^* = 100$ Hz and the absence of fluid flow out of the sample (i.e., $B^* \to 0$) at $f^* = 200$ Hz (i.e., Figure 12b).

From Table 1, the undrained/unrelaxed transition's cutoff frequency can also be calculated. Its value is $f_2^* \sim 1$ kHz. The apparatus does not allow to measure K_{LF} at such frequency. Yet, K_{HF} was measured using the ultrasonic velocity setup at $f \sim 0.5$ MHz. Its much higher value (i.e., approximately ~34 GPa) is likely to be related to a transition from undrained to unrelaxed regimes.

Case of Fo9 sample: An exotic behavior

Fo9 data measured at $P_{eff} \sim 1$ MPa are reported as a function of f^* (Figure 17). Again, a clear increase in K_{LF} is observed as f^* increases (Figure 17a).

However, considering the low f^* value of K_{LF} (i.e., 25 GPa) to be the value for the drained modulus K_d, the Biot-Gassmann undrained prediction is $K_u = 29$ GPa. In this case, the Biot-Gassmann prediction underestimates the increase in K_{LF} with f^*. In addition, ultrasonic data lead to a K_{HF} value close to the one of K_{LF} at $f^* = 500$ Hz. It implies that no frequency effect exists in the range of $f^* \in [500\text{ Hz} - 0.5\text{ MHz}]$. This behavior shows that the bulk modulus increases directly from the drained modulus (at lowest

Table 1. Specific properties measured for both samples at an effective pressure of $P_{eff} \sim 1$ MPa.

Sample no.	Fo9	Fo7
Porosity ϕ	8.7%	7.2%
Diffusion length L	40–80 mm	40–80 mm
Permeability κ	1.10^{-14} m^2	4.10^{-15} m^2
Drained bulk modulus K_d	25 GPa	15 GPa
Aspect ratio ξ	$1 - 2.10^{-4}$	$4 - 5.10^{-4}$
Frequency f_1^*	156–625 Hz	35–140 Hz
Frequency f_2^*	25–200 Hz	1000–2000 Hz

frequency) up to the unrelaxed modulus (at $f^* \sim 500$ Hz). For this sandstone, the undrained regime does not seem to exist. This behavior implies that f_1^* and f_2^* values overlap in the frequency range of K_{LF} variation, which is consistent with the values predicted for f_1^* and f_2^* (Table 1). This is unusual because one expects in general $f_1^* \ll f_2^*$. This is, however, because $L \ll \lambda$ in our case, where λ is the wavelength, so that it can be possible to have a "drained" sample. Our result implies that Fo9 presents a special case for which the undrained regime does not exist (in our experimental conditions). This unusual case has been considered previously by Cleary (1978).

Variation in attenuation with frequency

From Figures 11a and 11b, a progressive increase in K_{LF} with frequency is measured in Fo9 and Fo7 that indicates a progressive transition between domains, and Q_K^{-1} data show a good correlation with K_{LF} variations with frequency. At that point, the Zener viscoelastic model (e.g., Nowick and Berry, 1972) can be used. Parameters are the springs moduli M_a and M_b, and the dashpot viscosity η_b (Figure 15), which can be directly inferred from the problem's parameters. The dashpot viscosity η_b could be derived from the relaxation time $\tau_0 = \eta_b / M_b$, which directly relates to the critical frequency such that $\tau_0^{-1} = 2\pi f_c$.

By combining Zener model and Biot-Gassmann prediction, one obtains a possible transition in bulk modulus dispersion and attenuation from drained to undrained conditions (Figure 18); M_b is taken as the drained modulus K_d, i.e., 16 and 25 GPa for Fo7 and Fo9, respectively. Knowing M_b, M_a is deduced from the undrained modulus K_u determined from the Biot-Gassmann equation (Equation 3) in the case of glycerin full saturation. A value of η_b is chosen as a best fit of the characteristic frequency of measurements' variations. For Fo7, K_{LF} and Q_K^{-1} variations with frequency indicate a typical Zener-like drained/undrained transition (Figure 18b and 18d). For Fo9, however, the Zener-like drained/undrained transition underestimates the dispersion and attenuation measured. This may originate from the overlapping critical frequencies (Table 1 and Figure 17).

The Zener model can also be used to describe the transition from undrained to unrelaxed conditions. This result is presented for Fo7 at four different P_{eff} (Figure 19): The predicted attenuation curves are obtained assuming that the drained/undrained frequency effect relates to a K increase from K_d to K_u and the relaxed/unrelaxed frequency effect relates to a K increase from K_u up to K_{HF}. At $P_{eff} \sim 1$ MPa (Figures 18d and 19a), predicted and measured attenuation are in good agreement for the first transition. It appears also that Q_K^{-1} peak due to the drained/undrained transition is larger than the one associated with the relaxed/unrelaxed transition.

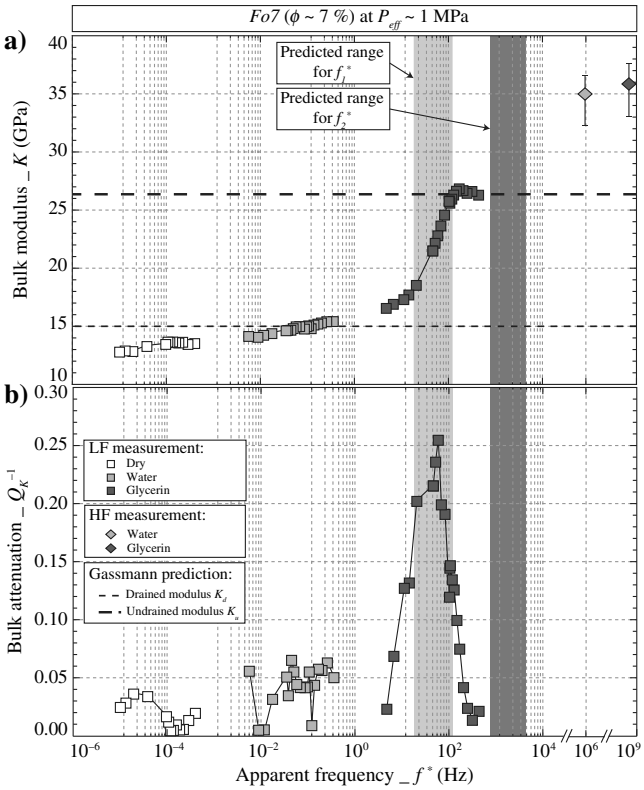

Figure 16. (a) Fo7 LF bulk modulus K_{LF} and (b) attenuation Q_K^{-1} versus f^* at an effective pressure of $P_{eff} \sim 1$ MPa. The Biot-Gassmann theory for drained and undrained bulk moduli prediction (i.e., dashed lines) and the measured K_{HF} (i.e., diamonds) are also reported. The ranges for the theoretical cutoff frequencies f_1^* and f_2^*, reported in Table 1, are shown by means of grayish zones.

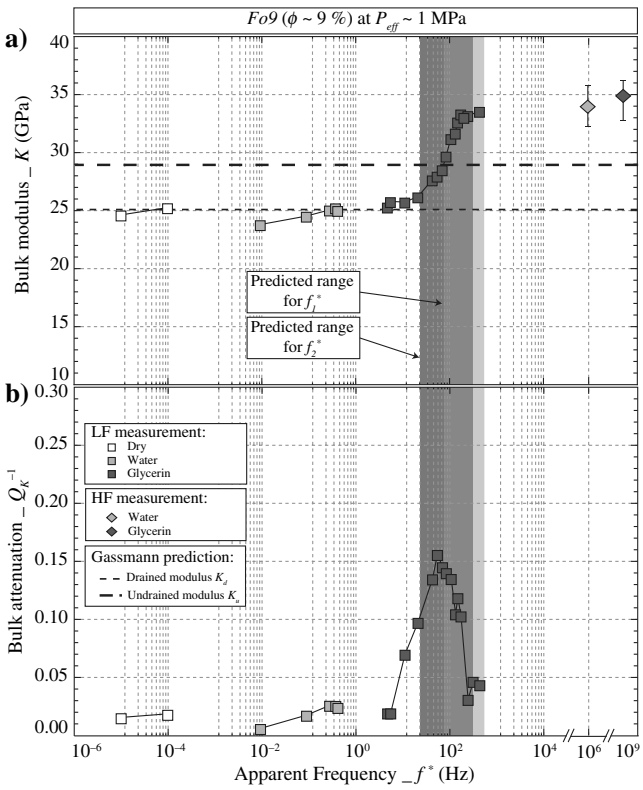

Figure 17. (a) Fo9 LF bulk modulus K_{LF} and (b) attenuation Q_K^{-1} versus f^* at an effective pressure of $P_{eff} \sim 1$ MPa. The Biot-Gassmann theory for drained and undrained bulk moduli prediction (i.e., dashed lines) and the measured K_{HF} (i.e., diamonds) are also reported. The ranges for the theoretical cutoff frequencies f_1^* and f_2^*, reported in Table 1, are shown by means of grayish zones.

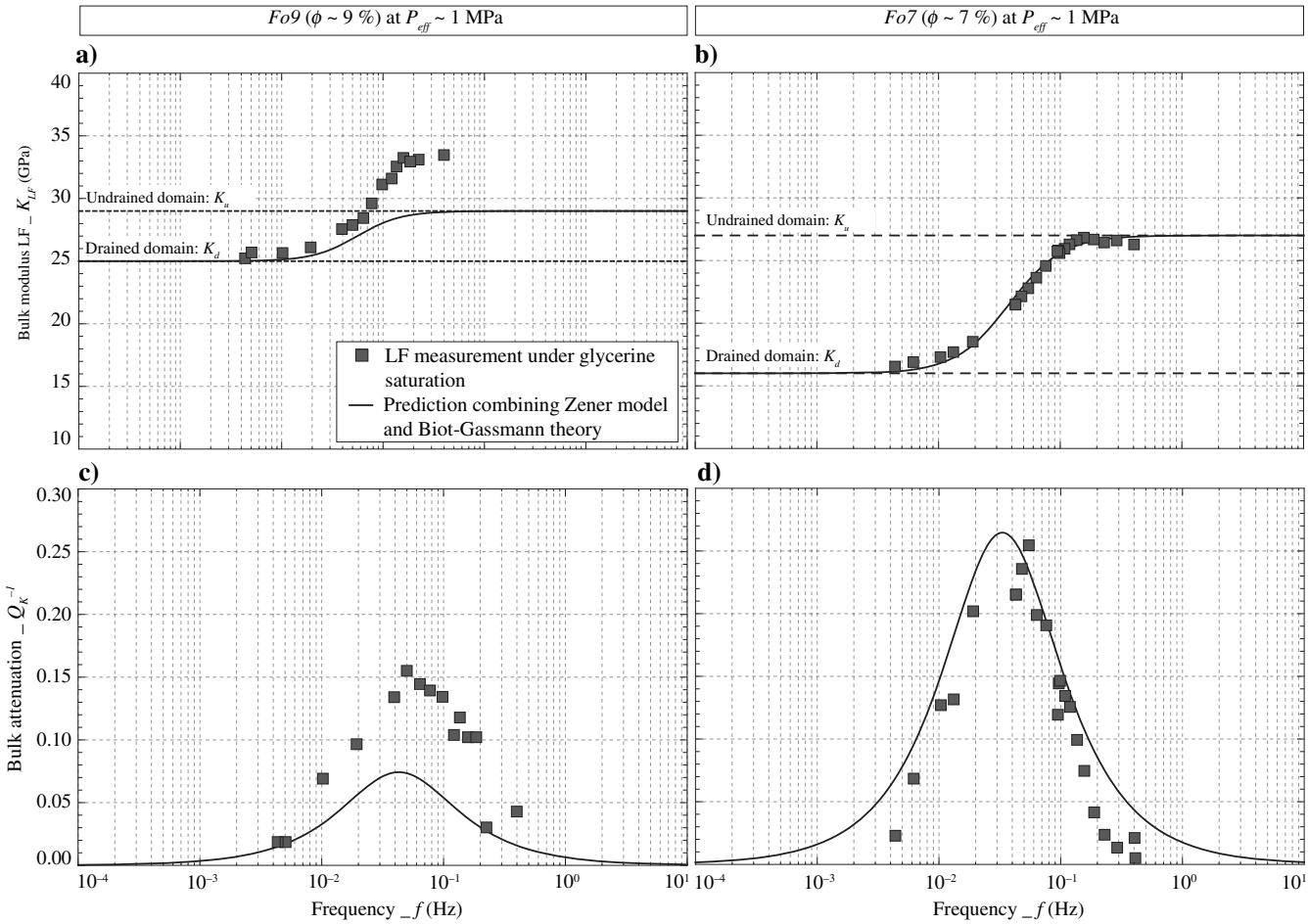

Figure 18. Comparison between measured and predicted (a) bulk modulus and (b) attenuation variations with frequency in the glycerin-saturated Fo7. The prediction is obtained by combining the Zener rheological model and the Biot-Gassmann theory.

Attenuation is progressively damped by the pressure increase up to $P_{\text{eff}} \sim 30$ MPa (Figure 19d). Comparing drained/undrained and relaxed/unrelaxed transitions, P_{eff} modifies particularly the drained/undrained transition, with a variation in attenuation peak from $Q_K^{-1} \sim 0.25$ down to approximately $Q_K^{-1} \sim 0.03$. This strong effect of pressure is the result of the cracks' closure. The undrained K_u depends on the drained K_d, which in turn highly depends on pressure-sensitive cracks (e.g., Guéguen and Kachanov, 2011). As the pressure increases, K_d increases and the difference between K_u and K_d decreases. This pressure effect on dispersion corresponding to the drained/undrained is thus expected and implicitly accounted for by the Biot-Gassmann theory. Using the Zener model proves to be satisfactory. Attenuation peak amplitudes and modulus variations are indeed consistent, and they both decrease when P_{eff} increases. At higher P_{eff} values, the agreement between Biot-Gassmann model predictions and data is not as good as at low P_{eff}. Note, however, that the effects are much smaller.

CONCLUSION

We report new data on bulk modulus dispersion and attenuation in fully saturated sandstone samples. The capabilities of the apparatus have been checked using three reference samples: glass, gypsum, and Plexiglas. The frequency range allowed for the measurement is $f \in [4.0\ 10^{-3}; 4.0\ 10^{-1}]$ Hz. The setup has been used to measure frequency effects in two Fontainebleau samples of ~9% (Fo9) and ~7% (Fo7) porosity. In addition to the measurement under dry conditions, two different saturating fluids have been used: water and glycerin. Owing to their relative viscosities, the apparent frequency range of study has been extended for these sandstone samples to $f^* \in [3.5\ 10^{-3}; 4.3\ 10^{2}]$ Hz.

The measured frequency dependence of bulk modulus and attenuation varies with the saturating fluid. Under dry and water-saturated conditions, the sample is fully drained. Under glycerin saturation, a large frequency-dependent increase is measured on K_{LF} and Q_K^{-1}, with attenuation peaks as high as approximately 0.15 and 0.25 for Fo9 and Fo7, respectively. Confining pressure appears to highly damp these frequency effects. Monitoring the fluid flow out of the samples, in terms of a pseudo-Skempton coefficient, allows to gain further insights into the frequency effect. Fluid is observed to flow out of the samples under water and glycerin saturation at lower frequency, implying that the samples are drained. Oppositely, in glycerin-saturated samples, the flow is observed to decrease with frequency and even vanish at higher frequency. In other words, the samples are undrained.

Combining the Zener viscoelastic model and the Biot-Gassmann theory, the measurements on the glycerin-saturated samples are compared to predictions for the drained/undrained transition. Fo7

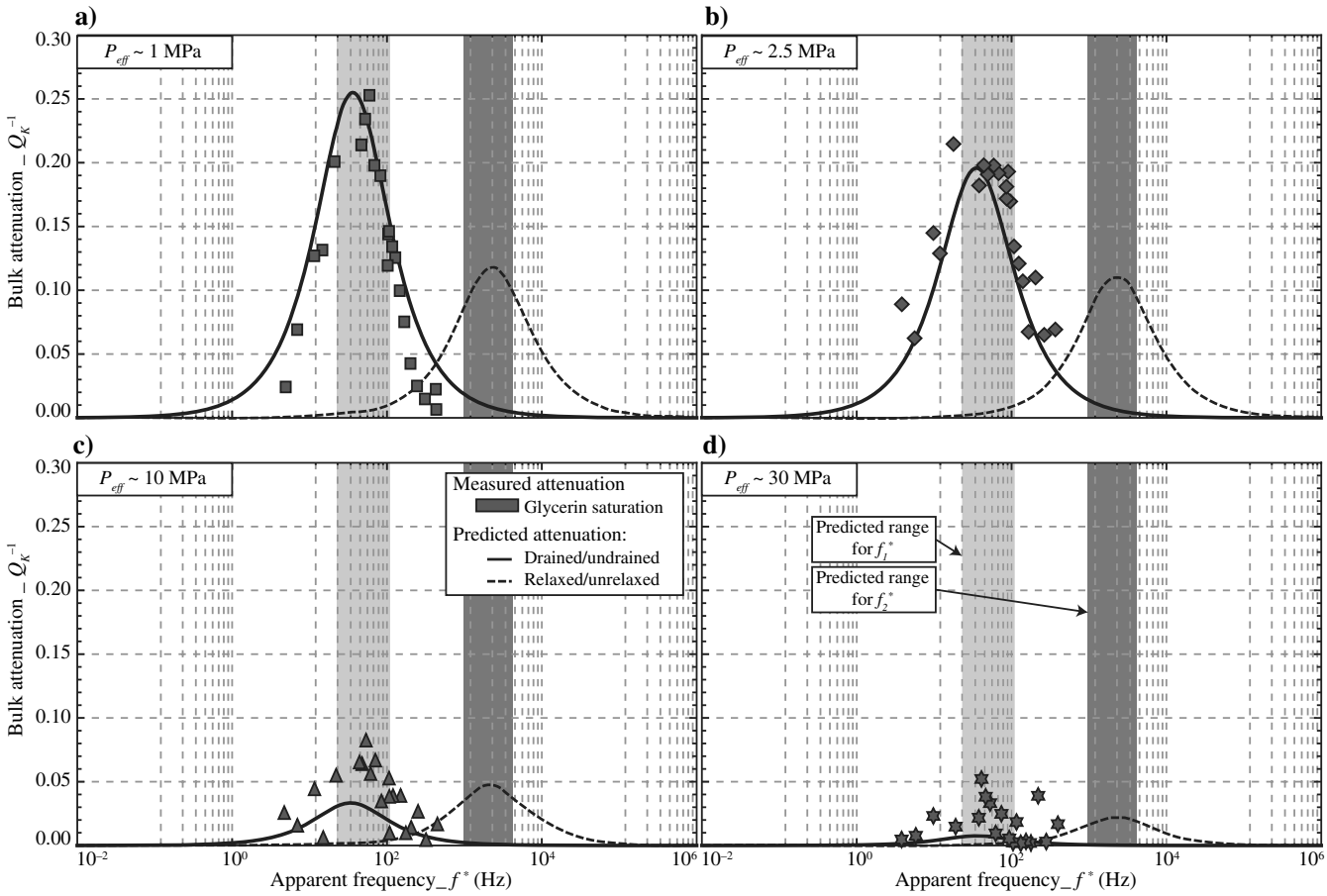

Figure 19. (a) Comparison between predicted and measured attenuation curves for Fo7 for $P_{\text{eff}} \sim 1$ MPa, (b) $P_{\text{eff}} \sim 2.5$ MPa, (c) $P_{\text{eff}} \sim 10$ MPa, and (d) $P_{\text{eff}} \sim 30$ MPa. The theoretical cutoff frequencies are introduced by means of grayish zones.

data are in good agreement with the predictions, implying that the frequency effect measured corresponds to the drained/undrained transition. Oppositely, the prediction clearly underestimates the dispersion and attenuation measured on Fo9, indicating that the measurement cannot be strictly related to a drained/undrained transition but involves the relaxed/unrelaxed transition.

Fo7 and Fo9 bulk moduli and attenuation show critical frequency values in agreement with the data. In the case of Fo9, an unusual result is reported: a direct transition from drained to unrelaxed. Attenuation associated with the drained/undrained transition is larger in Fo7 than the one associated with the relaxed/unrelaxed transition (i.e., squirt flow). Attenuation associated with the drained/undrained transition is more pressure sensitive than the one associated with the relaxed/unrelaxed transition. At $P_{\text{eff}} \sim 30$ MPa, these effects are vanishingly small for Fo7 and Fo9.

ACKNOWLEDGMENTS

The authors would like to thank A. Schubnel and Y. Pinquier for their help on the experimental setup. M. Lebedev, J. Sarout, and an anonymous reviewer are thanked for their constructive comments. L. Pimienta also wishes to thank P. Maury for her help with the data processing.

REFERENCES

Adam, L., M. Batzle, and I. Brevik, 2006, Gassmann's fluid substitution and shear modulus variability in carbonates at laboratory seismic and ultrasonic frequencies: Geophysics, **71**, no. 6, F173–F183, doi: 10.1190/1.2358494.

Adelinet, M., J. Fortin, and Y. Gueguen, 2011, Dispersion of elastic moduli in a porous-cracked rock: Theoretical predictions for squirt-flow: Tectonophysics, **503**, 173–181, doi: 10.1016/j.tecto.2010.10.012.

Adelinet, M., J. Fortin, Y. Guéguen, A. Schubnel, and L. Georoy, 2010, Frequency and fluid effects on elastic properties of basalt: Experimental investigations: Geophysical Research Letters, **37**, L02303, doi: 10.1029/2009GL041660.

Barrau, J.-J., and S. Laroze, 1988, Mécanique des structures: Tome 1, Masson.

Batzle, M., R. Hofmann, D.-H. Han, and J. Castagna, 2001, Fluids and frequency dependent seismic velocity of rocks: The Leading Edge, **20**, 168–171, doi: 10.1190/1.1438900.

Batzle, M. L., D.-H. Han, and R. Hofmann, 2006, Fluid mobility and frequency-dependent seismic velocity direct measurements: Geophysics, **71**, no. 1, N1–N9, doi: 10.1190/1.2159053.

Bourbie, T., and B. Zinszner, 1985, Hydraulic and acoustic properties as a function of porosity in Fontainebleau sandstone: Journal of Geophysical Research: Solid Earth, **90**, 11524–11532., doi: 10.1029/JB090iB13p11524.

Brantut, N., A. Schubnel, E. David, E. Héripré, Y. Guéguen, and A. Dimanov, 2012, Dehydration-induced damage and deformation in gypsum and implications for subduction zone processes: Journal of Geophysical Research: Solid Earth, **117**, B03205., doi: 10.1029/2011JB008730.

Cleary, M. P., 1978, Elastic and dynamic response regimes of fluid-impregnated solids with diverse microstructures: International Journal of Solids and Structures, **14**, 795–819, doi: 10.1016/0020-7683(78)90072-0.

David, E. C., J. Fortin, A. Schubnel, Y. Guéguen, and R. W. Zimmerman, 2013, Laboratory measurements of low-and high-frequency elastic moduli in Fontainebleau sandstone: Geophysics, **78**, no. 5, D369–D379, doi: 10.1190/geo2013-0070.1.

Fortin, J., Y. Guéguen, and A. Schubnel, 2007, Effects of pore collapse and grain crushing on ultrasonic velocities and V_p/V_s: Journal of Geophysical Research: Solid Earth, **112**, 1978–2012, doi: 10.1029/2005JB004005.

Fortin, J., L. Pimienta, Y. Guéguen, A. Schubnel, E. David, and M. Adelinet, 2014, Experimental results on the combined effects of frequency and pressure on the dispersion of elastic waves in porous rocks: The Leading Edge, **33**, 648–654, doi: 10.1190/tle33060648.1.

Fortin, J., A. Schubnel, and Y. Guéguen, 2005, Elastic wave velocities and permeability evolution during compaction of Bleurswiller sandstone: International Journal of Rock Mechanics and Mining Sciences, **42**, 873–889, doi: 10.1016/j.ijrmms.2005.05.002.

Gassmann, F., 1951, On the elasticity of porous media: Vierteljahrsschrder Naturforschenden Gesselschaft, **96**, 1–23.

Gomez, C., J. Dvorkin, and T. Vanorio, 2010, Laboratory measurements of porosity, permeability, resistivity, and velocity on Fontainebleau sandstones: Geophysics, **75**, no. 6, E191–E204, doi: 10.1190/1.3493633.

Guéguen, Y., and M. Kachanov, 2011, Effective elastic properties of cracked rocks — An overview, *in* Y. Leroy, and F. K. Lehner, eds., Mechanics of crustal rocks, CSIM courses and lectures: Springer, vol. 533, 73–125, .

Jackson, I., and M. Paterson, 1987, Shear modulus and internal friction of calcite rocks at seismic frequencies: Pressure, frequency and grain size dependence: Physics of the Earth and Planetary Interiors, **45**, 349–367, doi: 10.1016/0031-9201(87)90042-2.

Madonna, C., and N. Tisato, 2013, A new seismic wave attenuation module to experimentally measure low-frequency attenuation in extensional mode: Geophysical Prospecting, **61**, 302–314, doi: 10.1111/1365-2478.12015.

Mallet, C., J. Fortin, Y. Guéguen, and F. Bouyer, 2013, Effective elastic properties of cracked solids: An experimental investigation: International Journal of Fracture, **182**, 275–282, doi: 10.1007/s10704-013-9855-y.

Mavko, G., T. Mukerji, and J. Dvorkin, 2003, The rock physics handbook: Tools for seismic analysis of porous media: Cambridge University Press.

Mikhaltsevitch, V., M. Lebedev, and B. Gurevich, 2014, A laboratory study of low-frequency wave dispersion and attenuation in water-saturated sandstones: The Leading Edge, **33**, 616–622, doi: 10.1190/tle33060616.1.

Müller, T. M., B. Gurevich, and M. Lebedev, 2010, Seismic wave attenuation and dispersion resulting from wave-induced flow in porous rocks — A review: Geophysics, **75**, no. 5, A147–A164, doi: 10.1190/1.3463417.

Nowick, A., and B. Berry, 1972, Anelastic relaxation in crystalline solids: Academic.

O'Connell, R. J., and B. Budiansky, 1974, Seismic velocities in dry and saturated cracked solids: Journal of Geophysical Research, **79**, 5412–5426, doi: 10.1029/JB079i035p05412.

O'Connell, R. J., and B. Budiansky, 1977, Viscoelastic properties of fluid-saturated cracked solids: Journal of Geophysical Research, **82**, 5719–5735, doi: 10.1029/JB082i036p05719.

Ougier-Simonin, A., J. Fortin, Y. Gueguen, A. Schubnel, and F. Bouyer, 2011, Cracks in glass under triaxial conditions: International Journal of Engineering Science, **49**, 105–121, doi: 10.1016/j.ijengsci.2010.06.026.

Ravalec, M. L., Y. Gueguen, and T. Chelidze, 1996, Elastic wave velocities in partially saturated rocks: Saturation hysteresis: Journal of Geophysical Research, **101**, 837–844, doi: 10.1029/95JB02879.

Sarout, J., 2012, Impact of pore space topology on permeability, cut-off frequencies and validity of wave propagation theories: Geophysical Journal International, **189**, 481–492, doi: 10.1111/j.1365-246X.2011.05329.x.

Spencer, J., Jr., 1981, Stress relaxations at low frequencies in fluid-saturated rocks: Attenuation and modulus dispersion: Journal of Geophysical Research, **86**, 1803–1812, doi: 10.1029/JB086iB03p01803.

Subramaniyan, S., B. Quintal, N. Tisato, E. H. Saenger, and C. Madonna, 2014, An overview of laboratory apparatuses to measure seismic attenuation in reservoir rocks: Geophysical Prospecting, **62**, 1211–1223, doi: 10.1111/1365-2478.12171.

Tisato, N., and C. Madonna, 2012, Attenuation at low seismic frequencies in partially saturated rocks: Measurements and description of a new apparatus: Journal of Applied Geophysics, **86**, 44–53, doi: 10.1016/j.jappgeo.2012.07.008.

Walsh, J., 1965, The effect of cracks on the uniaxial elastic compression of rocks: Journal of Geophysical Research, **70**, 399–411, doi: 10.1029/JZ070i002p00399.

Winkler, K., 1985, Dispersion analysis of velocity and attenuation in Berea sandstone: Journal of Geophysical Research, **90**, 793–796., doi: 10.1029/JB090iB08p06793.

Winkler, K. W., and W. F. Murphy III, 1995, Acoustic velocity and attenuation in porous rocks, *in* T. J. Ahrens, ed., Rock Physics and phase relations — A handbook of physical constants, American Geophysical Union, AGU Reference Shelf 3.